

Moderate Reynolds number flows through periodic and random arrays of aligned cylinders

By DONALD L. KOCH¹ AND ANTHONY J. C. LADD²

¹School of Chemical Engineering, Cornell University, Ithaca, NY 14853, USA

²Lawrence Livermore National Laboratory, Livermore, CA 94550, USA

(Received 13 November 1996 and in revised form 16 May 1997)

The effects of fluid inertia on the pressure drop required to drive fluid flow through periodic and random arrays of aligned cylinders is investigated. Numerical simulations using a lattice-Boltzmann formulation are performed for Reynolds numbers up to about 180.

The magnitude of the drag per unit length on cylinders in a square array at moderate Reynolds number is strongly dependent on the orientation of the drag (or pressure gradient) with respect to the axes of the array; this contrasts with Stokes flow through a square array, which is characterized by an isotropic permeability. Transitions to time-oscillatory and chaotically varying flows are observed at critical Reynolds numbers that depend on the orientation of the pressure gradient and the volume fraction.

In the limit $Re \ll 1$, the mean drag per unit length, F , in both periodic and random arrays, is given by $F/(\mu U) = k_1 + k_2 Re^2$, where μ is the fluid viscosity, U is the mean velocity in the bed, and k_1 and k_2 are functions of the solid volume fraction ϕ . Theoretical analyses based on point-particle and lubrication approximations are used to determine these coefficients in the limits of small and large concentration, respectively.

In random arrays, the drag makes a transition from a quadratic to a linear Re -dependence at Reynolds numbers of between 2 and 5. Thus, the empirical Ergun formula, $F/(\mu U) = c_1 + c_2 Re$, is applicable for $Re > 5$. We determine the constants c_1 and c_2 over a wide range of ϕ . The relative importance of inertia becomes smaller as the volume fraction approaches close packing, because the largest contribution to the dissipation in this limit comes from the viscous lubrication flow in the small gaps between the cylinders.

1. Introduction

This paper addresses fluid flow through periodic and random arrays of aligned cylinders. The effects of fluid inertia on the pressure drop required to drive the flow will be determined for Reynolds numbers, $Re = 2\rho Ua/\mu$, between 0 and 180. Here, ρ and μ are the fluid density and viscosity, a is the radius of the cylinders, and U is the average velocity throughout the bed. A fluid flow through a periodic array of cylinders arises on the shell side of a heat exchanger. While the Reynolds numbers in most heat exchangers are larger than those investigated here, pin fin heat exchangers with $Re = 10$ –100 have been proposed as a means of cooling electronic components (Fisher, Torrance & Sikka 1997). Hollow-fibre filters contain disordered arrays of aligned fibres and the Reynolds number of the shell-side flow is typically 1–10. In many other fibrous

filters such as those used to remove airborne particulates, the fibres are not aligned, but the current investigation still provides a first step toward understanding the finite Reynolds number flow through these media. An important consideration in the design of heat exchangers and fibrous filters is the pressure drop/flow rate relationship and this will be the primary focus of the present investigation.

This study of flow in fixed arrays of cylinders also represents an interesting first step toward understanding the effects of fluid inertia on the behaviour of suspensions and fixed beds. While extensive theoretical and computational studies have been developed for a wide range of viscous suspension flows (Brady & Bossis 1988), studies that include inertia have largely been limited to suspensions in which the inertia is entirely in the particulate phase (Sangani *et al.* 1996), the flow is inviscid and irrotational (Sangani & Didwania 1993), or a modest number of particles are included in the computation (Feng, Hu & Joseph 1994). Fixed beds are a natural starting point for investigations of fluid inertia effects on the properties of particle dispersions, because it is not necessary to follow the evolution of the particulate-phase microstructure to obtain a statistical steady state in these systems. The two-dimensional nature of the flow in the present system also affords a significant economy of computational effort.

Extensive theoretical and computational studies have led to a quite thorough understanding of Stokes flow ($Re = 0$) in periodic and random arrays of aligned cylinders. Owing to the linearity of the Stokes equations of motion, the mean velocity U is proportional to the pressure gradient driving the flow at $Re = 0$. The coefficient of proportionality is a scalar (k/μ , where k is the permeability) when the medium is isotropic. The permeability is also a scalar in a simple square array of cylinders as a result of the principle of linear superposition. Hasimoto (1959) determined the permeability of simple square arrays of cylinders in the limit where the volume fraction of the cylinders is small. Sangani & Acrivos (1982) extended this analysis to arbitrary area fractions by including a large number of multipoles in the expansion for the velocity disturbance caused by the cylinders. They also provided an analytical solution for the permeability of highly concentrated arrays using lubrication theory to determine the large resistance to driving the fluid through the small gaps between the cylinders. The permeability was found to be proportional to $\epsilon^{5/2}$ in the limit $\epsilon \rightarrow 0$, where $a\epsilon$ is the gap between neighbouring cylinders. We will derive the first effects of fluid inertia on this lubrication flow.

Theoretical predictions for the permeabilities of dilute fixed beds can be obtained using a self-consistent approximation, in which the drag on a particle is evaluated using an equation of motion for the surrounding medium that includes a body force representing the drag on the surrounding particles. This approach was first pursued for fixed beds of spheres by Brinkman (1947) and later applied to arrays of aligned cylinders by Spielman & Goren (1968) and Howells (1974). In the context of the fixed bed of spheres, Hinch (1977) showed that such a self-consistent calculation yields the leading-order solution for small volume fractions of the ensemble-averaged equations of motion in the bed.

Numerical simulations of Stokes flow through arrays of randomly positioned, aligned cylinders were first performed by Sangani & Yao (1988) using a multipole representation of the velocity disturbance caused by each of the cylinders. Sangani & Mo (1994) performed more extensive simulations using a slightly more sophisticated method in which the lubrication interactions between cylinders separated by small distances are accounted for using multipole expansions about the centre of the lubrication gap in addition to the expansions around the centres of the particles. Ghaddar (1995) used a finite element method to determine the permeability. He

obtained results for a larger number of volume fractions but with slightly less statistical accuracy than Sangani & Mo (1994).

The literature concerning inertial flows is more limited. Edwards *et al.* (1990) and Ghaddar (1995) computed the fluid flow through periodic arrays of cylinders over a range of Reynolds numbers (0–180). Bittleston (1986) performed similar computations and obtained a favourable comparison between the computed streamline patterns and his experimental observations. However, the primary emphasis of these authors was on situations in which the pressure gradient was parallel to one of the primary axes of the periodic array. We will see that the nature of the flow depends strongly on the orientation of the pressure gradient relative to the primary axis of the array and the pressure gradient required to drive a given velocity is generally much larger for off-axis flows. Ghaddar (1995) also provided some limited results for inertial flows through random arrays of cylinders. However, the statistical accuracy of these results is poor because they were performed on arrays of 16 or fewer cylinders without any ensemble averaging. In an investigation conducted concurrently with our own, Noble, Georgiadis & Buckius (1997) obtained statistically accurate results for the pressure drop through random arrays of cylinders with octagonal cross-sections for Reynolds numbers up to 30 using a lattice-Boltzmann method. In addition to the pressure drop, Noble *et al.* also reported data for the fluid velocity distribution function and the conditional average velocity with one cylinder's position fixed.

Although there are no theoretical studies of the effect of inertia in two-dimensional porous media, there are two related studies. Tamada & Fujikawa (1957) derived the drag on a single row of periodically positioned cylinders for $Re \ll 1$ but $Re(H/a) = O(1)$. Here H is the spacing between the cylinders and the analysis was valid for $H \gg a$. This singular perturbation study considered a viscous-dominated inner region and an outer region where both viscous and inertial effects were important. We will pursue an analogous study of the drag in a simple square array of cylinders. Kaneda (1986) used an ensemble-averaged-equation approach to determine the drag in a dilute fixed bed of spheres when $Re \ll 1$ but $Re\phi^{-1/2} = O(1)$, so that inertia was negligible on the length scale of the particle radius but important on the scale of the Brinkman screening length. Here, ϕ is the solids volume fraction. We will perform an analogous study for a two-dimensional random porous media.

Most previous studies of fluid flow in suspensions and fixed beds have been based on methods in which the velocity field is expressed in terms of multipole expansions but these methods are only suitable for Stokes flow (Bossis & Brady 1988) or inviscid flows (Sangani & Didwania 1993). To simulate the incompressible Navier–Stokes equations at finite values of the Reynolds number, we will use the lattice-Boltzmann simulation method described in detail by Ladd (1994*a*). This method has been tested by comparing its predictions for a wide variety of Stokes flow problems with results of multipole methods and comparing the predictions for the finite-Reynolds-number flows past a single row of cylinders and through a cubic array of spheres with finite difference results (Ladd 1994*b*).

In §2, we give a brief description of the numerical method used in this study. Sections 3 and 4 contain results for periodic and random arrays of cylinders, respectively. In each of these sections, we first develop theoretical predictions for the first effects of inertia on the mean pressure gradient in the array (or, equivalently, the mean drag on the cylinders) at small Reynolds number and compare these theories with the results of numerical simulations. We then present numerical results for moderate Reynolds number.

2. Lattice-Boltzmann simulations

This section provides a brief description of the lattice-Boltzmann simulation method. A more thorough discussion of the method implemented in this paper is given in Ladd (1994*a*). We solve a Boltzmann equation for the one-particle velocity distribution function for a gas of molecules that translate from node to node on a cubic lattice with a discrete set of velocities \mathbf{c}_i . The distribution function $n_i(\mathbf{r}, t)$ describes the number density of molecules at node \mathbf{r} at time t that have a velocity \mathbf{c}_i . The mass density ρ , momentum density $\mathbf{j} = \rho\mathbf{u}$, and momentum flux $\mathbf{\Pi} = \rho\mathbf{u}\mathbf{u} - \mathbf{T}$ can be determined as moments of velocity distribution:

$$\rho = \sum_i n_i, \quad \mathbf{j} = \sum_i n_i \mathbf{c}_i, \quad \mathbf{\Pi} = \sum_i n_i \mathbf{c}_i \mathbf{c}_i. \quad (1)$$

Here \mathbf{u} is the mass average velocity and \mathbf{T} is the stress tensor. The computational utility of the lattice-Boltzmann equation is related to the observation that only a small number of discrete velocities are needed to provide a kinetic model that will produce the Navier–Stokes equations for the moments of the velocity distribution (Frisch, Hasslacher & Pomeau 1986). In the present model, there are 18 velocities that allow the molecules to move to the nearest and next-nearest neighbours of a simple cubic lattice in a single time step. Thus, there are six velocities of speed 1 corresponding to the (100) directions of the lattice and 12 velocities of speed $\sqrt{2}$ corresponding to the (110) directions.

The time evolution of the distribution functions n_i is described by a discrete analogue of the linearized Boltzmann equation (Ladd 1994*a*):

$$n_i(\mathbf{r} + \mathbf{c}_i, t + 1) = n_i(\mathbf{r}, t) + \Delta_i(n(\mathbf{r}, t)), \quad (2)$$

where Δ_i is the change of n_i due to the instantaneous molecular collisions occurring at the lattice nodes. All lengths are non-dimensionalized with the lattice spacing and times with the time step. The collision operator $\Delta(n)$ depends on all of the number densities n_i at the node denoted collectively as $n(\mathbf{r}, t)$. This collision operator is chosen to satisfy mass and momentum conservation and produce the Newtonian constitutive equation with the desired value of viscosity. The applied pressure gradient driving the flow is simulated as a constant body force that causes an increase in the momentum of fluid molecules at each node at each time step. After each collision, the molecules propagate to the next node $\mathbf{r} + \mathbf{c}_i$. Note that the evolution equations (2) are the discretized form of a set of linear partial differential equations. As in the standard kinetic theory of gases (Chapman & Cowling 1970), the nonlinear term $\nabla \cdot (\rho\mathbf{u}\mathbf{u})$ arises from deriving the moment equation corresponding to a linearized Boltzmann equation. The lattice-Boltzmann method is conceptually related to lattice-gas models (Ladd & Frankel 1990); however, the use of a Boltzmann formulation for the molecular velocity distribution function avoids the statistical fluctuations inherent in simulating the dynamics of individual lattice-gas molecules.

Each solid cylinder is defined by a circle of radius a_0 which cuts some of the links between lattice nodes. The fluid particles moving along these links interact with the solid surface at boundary nodes placed halfway along the links. Thus, a discrete representation of the particle surface is obtained, which becomes more circular as the particle-radius-to-node spacing ratio, a_0 , is made larger. A fluid particle impinging on a boundary node is reflected so that, in a single time step, it returns to the lattice node from which it came with an opposite velocity. As a result of the boundary node

interactions, the particle exerts a force on the fluid and the total force and torque acting on each particle as well as the local force per unit area are readily obtained from the simulation.

The discrete lattice causes the surface of the cylinder to be rough and thus its effective hydrodynamic radius, a , differs from the nominal radius, a_0 . We determined a by computing the drag on a dilute ($\phi < 0.1$) square array of cylinders in the limit of small Reynolds number and comparing the result with that of Sangani & Acrivos (1982). In this way it was determined that $a = a_0 + 0.3$ for all $a_0 = n + 0.5$ where n is an integer greater than 3. In some of the very dilute arrays, we also make use of cylinders with $a_0 = 2.5$, which corresponds to $a = 2.7$, and with $a_0 = 0.5$, which corresponds to $a = 0.61$. This effective radius is taken to be independent of fibre concentration and Reynolds number. Comparisons between results with different degrees of grid refinement and comparisons with results of other numerical methods confirm that a ϕ - and Re -independent effective radius adequately characterizes the effects of roughness over the range of Reynolds numbers investigated in this study.

The lattice-Boltzmann method reproduces the momentum and mass conservation equations for a Newtonian fluid. In its present formulation, however, it does not produce the correct energy equation. As a result, our results are restricted to low Mach numbers, $M = U/c_s \ll 1$, where $c_s = 1/\sqrt{2}$ is the speed of sound. In order to produce a large Reynolds number, $Re = 2aU/\nu$, we can use a large radius, a , and/or a small kinematic viscosity, ν . The collision rules can be adjusted to produce different values of ν . In most of our calculations $\nu = 0.01$. However, the viscosity and cylinder radius were varied for several representative simulations while maintaining a constant Re to assure that the effects of the discrete lattice and the compressibility of the lattice gas were small.

The size of the lattice required to obtain accurate results is primarily controlled by the need to resolve the flow in the gaps between neighbouring cylinders and to maintain a small Mach number (for fixed μ). The velocity of the fluid in the thin gaps between two cylinders is inversely proportional to the gap thickness and therefore the requirement of maintaining a small Mach number implies a minimum permissible value for the gap thickness. We found that about 10 lattice spacings across this gap provided accurate results (errors of less than about 3%) for $Re < 80$ in the periodic arrays and $Re < 40$ in the random arrays and that 20 lattice spacings allowed accurate calculations up to Reynolds numbers of about 180 in periodic and 80 in random arrays. The ratio of the maximum velocity to the mean velocity will be larger in a random than a periodic array and the computations are only accurate and stable if the Mach number based on the maximum velocity is small. This accounts for the more stringent requirement for grid resolution in random arrays.

We solved an initial value problem in which the fluid velocity was zero throughout the domain and a body force (or pressure gradient) was applied instantaneously at $t = 0$. The calculation was continued until the mean velocity (averaged over the volume of the bed) changed by less than 1% during the final 25% of the run. Because the transient was approximately exponential, this ensured that the difference between the reported value of the mean velocity and the long-time asymptote was less than 1%. In cases where the flow was unsteady, this criterion was applied to a temporally and spatially averaged velocity. Typically, 10000–40000 time steps were required, with slower transients occurring for larger non-dimensional gap thicknesses and smaller Reynolds numbers.

3. Square arrays of cylinders

3.1. Low Reynolds number behaviour

3.1.1. Numerical results for on-axis flows

To start, let us consider the first effects of fluid inertia on the flow in square arrays of cylinders. A force balance on the fluid in the bed at steady state indicates that the pressure gradient is equal to the product of the number of cylinders per unit area, $\phi/(\pi a^2)$, and the drag per unit length on each cylinder (or the mean drag in the case of unsteady flow or flow in a random array), which will be denoted as F . Thus, the results could be presented either in terms of pressure gradient or drag force and we will adopt the latter choice.

Mei & Auriault (1991) showed that the average drag acting on a particle in a porous medium with fore-aft symmetry at small Reynolds number contains a term proportional to the mean fluid velocity and a small inertial correction proportional to the product of the square of the Reynolds number and the mean velocity. If the array is random, then it is only required that the statistics of the structure have fore-aft symmetry. For the present example of a two-dimensional array, this corresponds to

$$\frac{F}{\mu U} = k_0 + k_2 Re^2 \quad \text{for } Re \ll 1. \quad (3)$$

In the present context, this result can be understood easily in terms of the fore-aft symmetry of the array and the properties of the Navier–Stokes equations:

$$\nabla^{*2} \mathbf{u}^* - \nabla^* p^* = Re \mathbf{u}^* \cdot \nabla^* \mathbf{u}^*, \quad (4)$$

$$\nabla^* \cdot \mathbf{u}^* = 0. \quad (5)$$

Here, $\mathbf{u}^* = \mathbf{u}/U$, $p^* = pa/\mu U$, and $\nabla^* = a\nabla$. If we expand the velocity and pressure in regular perturbation series, $\mathbf{u}^* = \mathbf{u}_0 + Re \mathbf{u}_1 + Re^2 \mathbf{u}_2$ and $p^* = p_0 + Re p_1 + Re^2 p_2$, then the leading-order velocity and pressure fields satisfy Stokes equations while the higher-order velocity and pressure fields contain inertial terms that depend on the lower-order velocity fields:

$$\nabla^{*2} \mathbf{u}_0 - \nabla^* p_0 = 0, \quad (6)$$

$$\nabla^{*2} \mathbf{u}_1 - \nabla^* p_1 = \mathbf{u}_0 \cdot \nabla^* \mathbf{u}_0, \quad (7)$$

$$\nabla^{*2} \mathbf{u}_2 - \nabla^* p_2 = \mathbf{u}_0 \cdot \nabla^* \mathbf{u}_1 + \mathbf{u}_1 \cdot \nabla^* \mathbf{u}_0, \quad (8)$$

$$\nabla^* \cdot \mathbf{u}_i = 0 \quad \text{for all } i. \quad (9)$$

The linearity of Stokes equations of motion, (6) and (9), together with the symmetry of the medium imply that \mathbf{u}_0 is an even function and p_0 an odd function of position. The right-hand side of (7) is an odd function of position, so that \mathbf{u}_1 is odd and p_1 is even. As a result, the $O(Re)$ contribution to the force per unit area acting on the surface of the cylinder, $\mathbf{n} \cdot [\mu(\nabla \mathbf{u}_1 - \nabla \mathbf{u}_1^\dagger) - p_1 \mathbf{I}]$, is an odd function of position and there is no net $O(Re)$ contribution to the force on the cylinder. In a similar manner, it can be seen that \mathbf{u}_2 is even and p_2 is odd, so that there is an $O(Re^2)$ correction to the force.

Our computations confirm (3). For example, the force per unit length acting on each cylinder in a square array of volume fraction $\phi = 0.2$ when the mean velocity is parallel to the primary axis of symmetry of the array (on-axis flow) is compared with (3) in

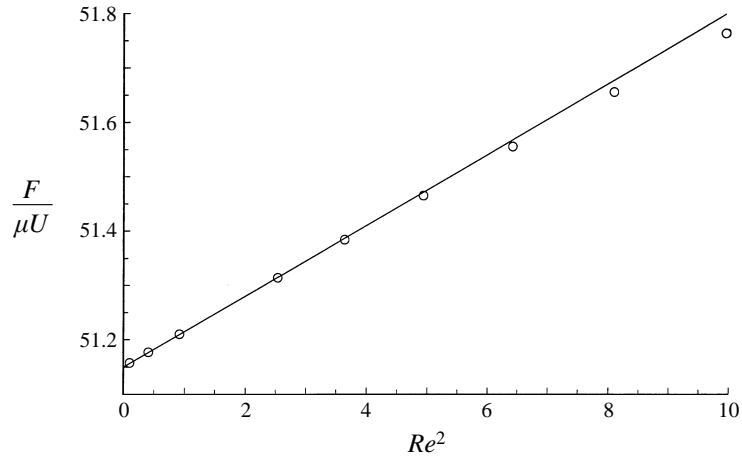


FIGURE 1. The force per unit length on a cylinder in a square array at low Reynolds numbers (circles) is compared with the asymptotic form (3) (line) with $k_0 = 51.19$ and $k_2 = 0.065$. The cylinder radius was $a = 9.8$.

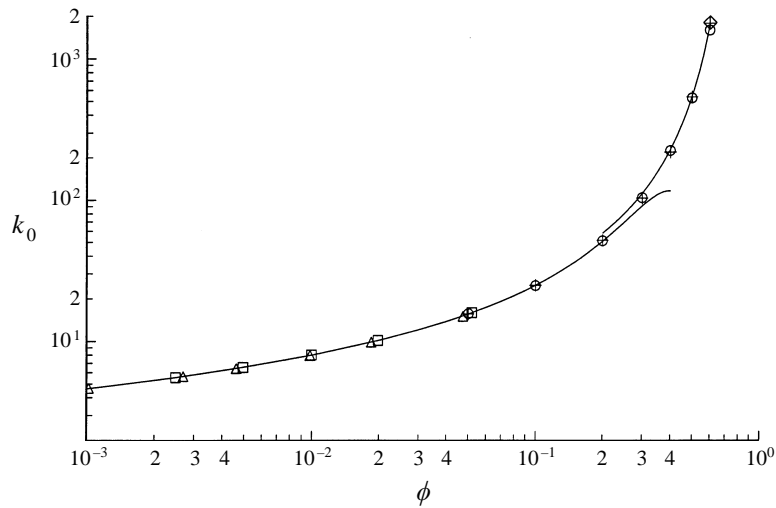


FIGURE 2. The force per unit length on a cylinder in a simple square array at zero Reynolds number is plotted as a function of the volume fraction ϕ . k_0 is the force per unit length non-dimensionalized by μU . \circ , Computations with 10 lattice nodes across the gap between particles; \diamond , a refined mesh, with 20 nodes across the gap; \square , \triangle , computations for dilute arrays with $a = 2.7$ and $a = 0.61$, respectively; lines, (10) and (12), i.e. the low- and high- ϕ asymptotes of Sangani & Acrivos (1982); +, computational results of Sangani & Acrivos (1982).

figure 1. By performing a similar regression analysis for the drag on cylinders due to on-axis flow over a range of volume fractions, we obtained the coefficients $k_0(\phi)$ and $k_2(\phi)$ plotted in figures 2 and 3, respectively. At moderate and large volume fractions, $\phi \geq 0.05$, the lattice was chosen so that there would be 10 nodes in the gap between neighbouring particles and the corresponding results are plotted as circles in figures 2 and 3. The diamond corresponds to an array with $\phi = 0.6$ and 20 nodes across the gap. In order to produce arrays with very small volume fractions, some calculations were done with quite small cylinder radii of $a = 2.7$ (squares) and $a = 0.61$ (triangles). The solid lines are theoretical predictions that will be described below.

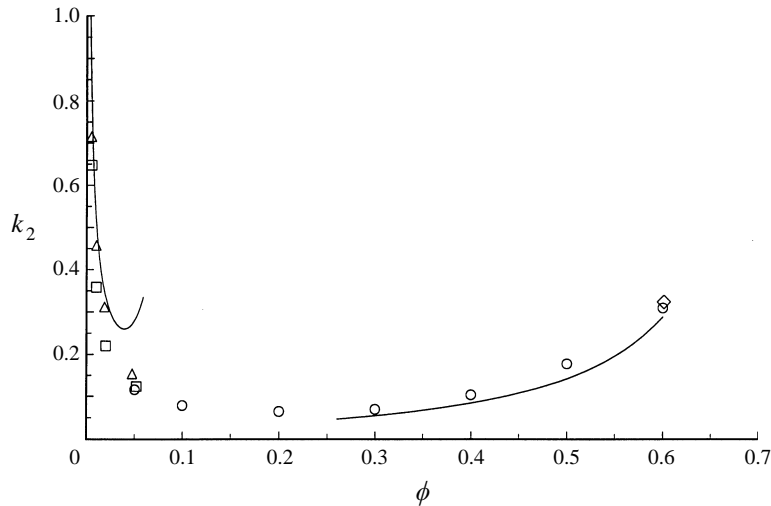


FIGURE 3. The coefficients k_2 defined in (3) is plotted as a function of volume fraction for a simple square array. The symbols are as defined in figure 2. The curves are the theoretical results, (32) and (13) for low and high ϕ , respectively.

The results for the drag at zero Reynolds number (k_0) can be compared with multipole solutions of Stokes equations of motion obtained by Sangani & Acrivos (1982). The lattice-Boltzmann computations with 10 nodes across the gap (circles in figure 2) are within 3% of the multipole results (crosses) except at the highest volume fraction $\phi = 0.6$ where the error is 11%. However, increasing the number of nodes across the gap to 20 (diamond) reduces the error to 1% for the most concentrated array $\phi = 0.6$.

Sangani & Acrivos (1982) also obtained a dilute approximation to the multipole expansion that can be expressed analytically as

$$k_0 = \frac{4\pi}{\ln(\phi^{-1/2}) - 0.738 + \phi - 0.887\phi^2 + 2.038\phi^3 + O(\phi^4)}. \quad (10)$$

Equation (10) is plotted as the first solid line in figure 2. Despite the small radius of the cylinders ($a = 2.7$ and 0.61) used at the smaller volume fractions, the agreement between this dilute asymptote and the data is excellent. This good agreement may be rationalized as follows. The analytical solution for very low volume fractions can be obtained from a singular perturbation analysis in which the inner solution corresponds to flow around a single cylinder and the outer solution corresponds to a periodic array of point forces. In the computations, we have adjusted the effective hydrodynamic radius, a , to obtain the appropriate inner solution. The outer solution is insensitive to the shape of the particle.

3.1.2. Theory for concentrated arrays

When the volume fraction is near the close packing limit, the requirement that all of the fluid flow through the small gaps between neighbouring particles leads to very high velocities and pressure drops in these gaps. The pressure drop across each gap may be derived by performing lubrication analyses on (6)–(9). Sangani & Acrivos (1982) solved the Stokes flow equations (6) and (9) to determine the leading contribution to the pressure drop at low Reynolds number. We will denote the gap thickness as $a\varepsilon$, where $\varepsilon = 1 - (4\phi/\pi)^{1/2}$ for a simple square array. Since all the fluid must flow through the

small gap, the characteristic value of the velocity component parallel to the gap, u_x , is U/ε . Here, x and y are Cartesian coordinates oriented along the principle axes of the square array. The width of the gap in the y -direction is $a\varepsilon$ while its length in the x -direction is $a\varepsilon^{1/2}$. The magnitude of the pressure gradient at zero Reynolds number is obtained by balancing the pressure gradient, $\partial p/\partial x = O(p/a\varepsilon^{1/2})$, with the viscous stress, $\mu\partial^2 u_x/\partial y^2 = O(\mu U/a^2\varepsilon^3)$. In this way, we find that $\Delta p = O(\mu U/a\varepsilon^{5/2})$. To obtain the first effects of inertia on this pressure drop, we have solved equations (7), (8), and (9). The inertial term $\rho\mathbf{u}\cdot\nabla\mathbf{u} = O(\rho U^2/a\varepsilon^{5/2})$ is $O(Re\varepsilon^{1/2})$ smaller than the viscous stress. The Reynolds number measures the relative importance of inertia and viscosity in the region outside the gap. Within the gap, the importance of inertia is increased by a factor of ε^{-1} due to the large velocity but is decreased by the same factor due to the small length scale. These two effects cancel and it is finally the nearly unidirectional nature of the flow that causes the inertial effects to be small like $Re\varepsilon^{1/2}$. As mentioned earlier, the first correction to the pressure field due to inertia is an even function of position and we must go to the $O(Re^2\varepsilon)$ problem to obtain a change in the net pressure drop. The pressure drop across the gap is

$$\Delta p_x = \frac{\mu U_x}{a\varepsilon^{5/2}} \left(\frac{9\pi}{4(2)^{1/2}} + \frac{39(2)^{1/2}\pi}{26950} Re_x^2 \varepsilon \right), \quad (11)$$

where U_x is the component of the mean velocity in the x -direction and $Re_x = 2a\rho U_x/\mu$. An analogous equation may be written for the pressure drop across gaps oriented in the y -direction. For the case of on-axis flow considered in figures 2 and 3, $U_x = U$ and $U_y = 0$. The leading contribution to the force on the particle comes from the difference in pressure Δp_x acting over the length, $2a$, of the cylinder's projection into the y -direction. Thus,

$$k_0 = \frac{9\pi}{2^{3/2}} \varepsilon^{-5/2} \quad (12)$$

and

$$k_2 = \frac{39(2)^{1/2}\pi}{13475} \varepsilon^{-3/2}. \quad (13)$$

These predictions of the lubrication analysis are plotted as the lines at high volume fractions in figures 2 and 3, respectively.

As mentioned earlier, the value of k_0 must be independent of the orientation of the flow relative to the primary axes of the array as a result of the linearity of Stokes flow. The inertial corrections to the relationship between the drag and the mean velocity need not have this isotropy and the drag force need not be aligned with the direction of the mean velocity at higher Reynolds numbers. Using (11), it is easy to show that the $O(Re^2)$ correction to the magnitude of the force, i.e. k_2 , is independent of the angle between the mean velocity and the x -axis, θ . However, the angle that the drag force makes with the x -axis, θ_F , is different from θ and is given by

$$\tan \theta = \tan \theta_F (1 + \beta Re^2) \quad \text{for } Re \ll 1, \quad (14)$$

where

$$\beta = \frac{52}{40425} \varepsilon \cos(2\theta_F), \quad (15)$$

Equation (15) indicates that the mean velocity in a highly concentrated array will be closer to a 45° angle away from each of the axes of the array than is the drag force or pressure gradient. One can rationalize this result by noting that there is a nonlinear increase in the pressure drop through the gap with increasing velocity. Thus, a greater incremental increase in the flow rate is obtained for the same increment of pressure drop in the set of gaps receiving the smaller fraction of the flow.

3.1.3. Theory for dilute arrays

Theoretical results for dilute arrays can be obtained through a singular perturbation analysis. The unit cell is divided into an inner region within an $O(a)$ distance from the particle and an outer region with a characteristic length scale of the interparticle spacing, $H = a(\pi/\phi)^{1/2}$. Hasimoto (1959) performed such an analysis under conditions of creeping flow in which inertia could be neglected in both the outer and inner regions. In the outer region, the finite size of the cylinders could be neglected and they were treated as point forces. In the inner region, the velocity could be approximated as that around a single cylinder. Matching these solutions provided a relationship between the mean velocity and the drag on the cylinder that corresponds to (10) if one neglects terms of $O(\phi)$ and higher.

As the flow rate is increased beyond the creeping flow regime, inertial effects first become important in the outer region because of its larger characteristic length. A simple theory can be obtained if one approximates the equations of motion in the outer region as Oseen's equations of motion. A more accurate prediction of the first effects of inertia can be obtained using the perturbation expansion (6)–(9) of the full Navier–Stokes equations. We will now discuss these two theories in turn.

The velocity disturbance produced by the cylinders at low Reynolds numbers is $O(1/\ln(H/a))$ smaller than the mean velocity throughout the outer region. Thus, with logarithmically small errors, one can approximate the momentum equation in the outer region by the Oseen equation:

$$\rho \mathbf{U} \cdot \nabla \mathbf{u} - \mu \nabla^2 \mathbf{u} + \nabla p = \mathbf{F} \sum_N \delta(\mathbf{x} - \mathbf{x}_N), \quad (16)$$

where \mathbf{x}_N is the position of the N th particle and the summation is over all the particles in the array. The linearity of the Oseen equation greatly simplifies the subsequent analysis. However, we shall see that the results are only accurate at exceedingly small volume fractions because of the $O(1/\ln(1/\phi))$ errors. A solution of (16) together with the mass conservation equation (5) may be obtained using Fourier transforms:

$$\mathbf{u} = \mathbf{U} + \frac{1}{H^2} \sum_{q \neq 0} \frac{\mathbf{F} \cdot (\mathbf{I} - \mathbf{q}\mathbf{q}/q^2)}{\mu(2\pi q)^2 + 2\pi i \rho \mathbf{q} \cdot \mathbf{U}} e^{2\pi i \mathbf{q} \cdot \mathbf{x}}, \quad (17)$$

where the summation is carried out over all the vectors of the reciprocal lattice. The fluid velocity may be written as

$$\mathbf{u} = \mathbf{U} + \mathbf{u}_s + \mathbf{u}_I, \quad (18)$$

where \mathbf{u}_s is the velocity disturbance caused by the particles in the absence of inertia and \mathbf{u}_I is the extra disturbance due to the inertial effects. Hasimoto showed that the Stokes flow velocity disturbance obtained from the outer solution behaves as

$$\mathbf{u}_s = \frac{\mathbf{F}}{4\pi\mu} \cdot \left(\mathbf{I} [\ln(H/x) - 1.3105] + \frac{\mathbf{x}\mathbf{x}}{x^2} - \frac{\mathbf{I}}{2} \right) \quad (19)$$

as one approaches one of the cylinders, i.e. $x \ll H$. The inertial velocity disturbance, which is obtained by subtracting the Fourier-space representation of the Stokes flow velocity field from (17), may be expressed as

$$\mathbf{u}_I(\mathbf{x} = 0) = -\mathbf{A} \cdot \mathbf{F}, \quad (20)$$

where

$$\mathbf{A} = \sum_{q \neq 0} \frac{4\pi Re_H^2 (\mathbf{I} - \mathbf{Q}\mathbf{Q}) (\mathbf{V} \cdot \mathbf{Q})^2}{(2\pi q)^4 + Re_H^2 (2\pi \mathbf{q} \cdot \mathbf{V})^2} \quad (21)$$

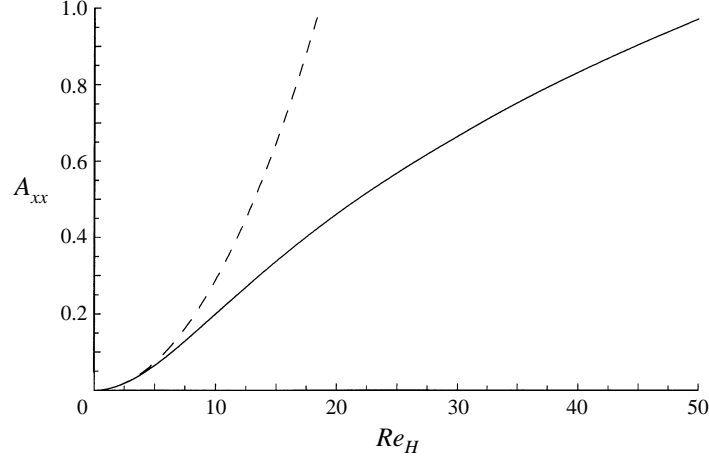


FIGURE 4. The Oseen theory for on-axis flows in dilute square arrays. The xx -component of the tensor \mathbf{A} appearing in the relationship (23) between the drag and the mean velocity is plotted as a function of Re_H . The dashed line indicates the low- Re_H asymptote, $A_{xx} = 2.90 \times 10^{-3} Re_H^2$.

and we have omitted an imaginary term that is odd and sums to zero. In (21), $\mathbf{Q} = \mathbf{q}/q$, $\mathbf{V} = \mathbf{U}/U$, \mathbf{q} has been scaled with H^{-1} and $Re_H = \rho UH/\mu$ is the Reynolds number based on the lattice spacing.

The inner solution obtained by solving Stokes flow around a single cylinder is

$$\mathbf{u}_{in}(x \gg a) = \frac{\mathbf{F}}{4\pi\mu} \cdot \left(\mathbf{I} \ln(a/x) + \frac{\mathbf{x}\mathbf{x}}{x^2} - \frac{\mathbf{I}}{2} \right). \quad (22)$$

A relationship between the mean velocity and the force can be obtained by matching the outer solution (18), (19), and (20) with the inner solution (22) to obtain

$$\mathbf{F} \cdot (b\mathbf{I} - \mathbf{A}) = -4\pi\mu U, \quad (23)$$

where $b = \frac{1}{2} \ln(1/\phi) - 0.738$ and \mathbf{A} is given by (21).

Equations (23) and (21) may be applied to cases in which the Reynolds number Re_H based on the lattice spacing is $O(1)$ provided that the Reynolds number, Re , based on the particle diameter is small. For the case of flow parallel to the primary axis of symmetry (x -axis), the velocity and force are in the x -direction and one need only consider the xx -component of the tensor \mathbf{A} . A_{xx} is plotted as a function of Re_H in figure 4. Initially, A_{xx} and therefore the force increase quadratically with Re_H . However, slower growth is obtained at $Re_H > 5$.

In the limit of small Re_H , one can neglect the $O(Re_H^2)$ term in the denominator of (21) and perform the sum to determine the coefficient k_2 defined in (3) to be

$$k_2 = \frac{4\pi \mathbf{V} \cdot \mathbf{A}_0 \cdot \mathbf{V}}{b^2}, \quad (24)$$

where

$$\mathbf{A}_0 = \sum_{q \neq 0} \frac{4\pi (\mathbf{V} \cdot \mathbf{K})^2 (\mathbf{I} - \mathbf{Q}\mathbf{Q})}{(2\pi q)^4}. \quad (25)$$

For flow parallel to the primary axis of the array

$$k_2 = \frac{0.0286}{\phi b^2}. \quad (26)$$

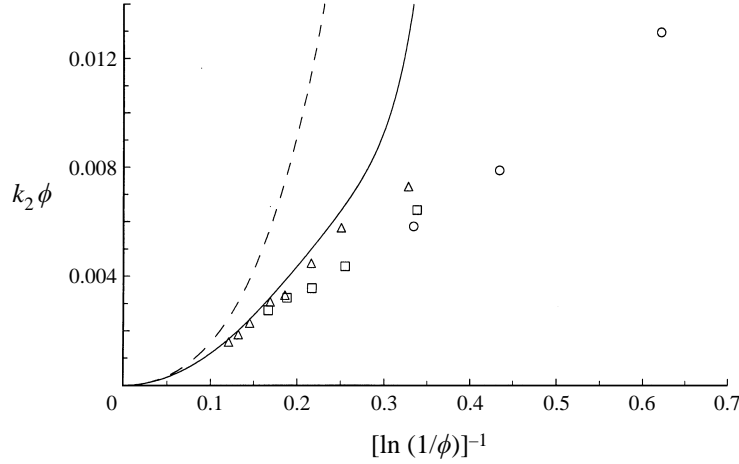


FIGURE 5. $k_2 \phi$ is plotted as a function of $[\ln(1/\phi)]^{-1}$ in order to compare the theories based on Oseen's equations of motion ((26), dashed line) and the Navier–Stokes equations ((32), solid line) with the computational results (symbols). The different symbols are as defined for figure 2.

The Oseen theory described above has $O(1/\ln(1/\phi))$ relative errors resulting from the linearization of the inertial term in the momentum equation. A more accurate theoretical prediction of the first effects of inertia on the drag can be obtained by solving the full Navier–Stokes equations in the outer region through an iterative procedure. The zero-order term in this expansion is obtained by solving (6) with an array of point forces on the right-hand side. The result for the Fourier transform of \mathbf{u}_0 is

$$\hat{\mathbf{u}}_0(\mathbf{q}) = \mathbf{F} \cdot \mathbf{J}(\mathbf{q}) \quad \text{for } \mathbf{q} \neq 0 \quad (27)$$

and $\hat{\mathbf{u}}_0 = 0$ for $\mathbf{q} = 0$. Here, \mathbf{J} is the Fourier transform of the Oseen tensor and is given by

$$\mathbf{J} = \frac{\mathbf{I} - \mathbf{Q}\mathbf{Q}}{\mu(2\pi q)^2}. \quad (28)$$

Solving the first- and second-order momentum equations after Fourier transforming yields

$$\hat{\mathbf{u}}_1(\mathbf{q}) = -2\pi i \mathbf{q} \cdot \mathbf{V} \mathbf{J}(\mathbf{q}) \cdot \hat{\mathbf{u}}_0(\mathbf{q}) - \sum_{\mathbf{q}'} \hat{\mathbf{u}}_0(\mathbf{q} - \mathbf{q}') \cdot 2\pi i \mathbf{q}' \mathbf{J}(\mathbf{q}) \cdot \hat{\mathbf{u}}_0(\mathbf{q}'), \quad (29)$$

$$\begin{aligned} \hat{\mathbf{u}}_2(\mathbf{q}) = & -2\pi i \mathbf{q} \cdot \mathbf{V} \mathbf{J}(\mathbf{q}) \cdot \hat{\mathbf{u}}_1(\mathbf{q}) - \sum_{\mathbf{q}'} [\hat{\mathbf{u}}_1(\mathbf{q} - \mathbf{q}') \cdot 2\pi i \mathbf{q}' \mathbf{J}(\mathbf{q}) \cdot \hat{\mathbf{u}}_0(\mathbf{q}') \\ & + \hat{\mathbf{u}}_0(\mathbf{q} - \mathbf{q}') \cdot 2\pi i \mathbf{q}' \mathbf{J}(\mathbf{q}) \cdot \hat{\mathbf{u}}_1(\mathbf{q}')]. \end{aligned} \quad (30)$$

This outer solution may be matched with the Stokes flow inner solution in a manner analogous to that outlined above for the Oseen theory. The evaluation of $\mathbf{u}_2(\mathbf{x} = 0)$ by inversion of the Fourier transform requires a six-dimensional summation and is therefore computationally intensive. In order to accelerate the convergence of the summation, we noted that the value of the velocity obtained by limiting the sum to $|q_x| < q_m$ and $|q_y| < q_m$ could be written as

$$\hat{\mathbf{u}}_{2x}(q_m) = u_{2x}(\infty) + B/q_m^2. \quad (31)$$

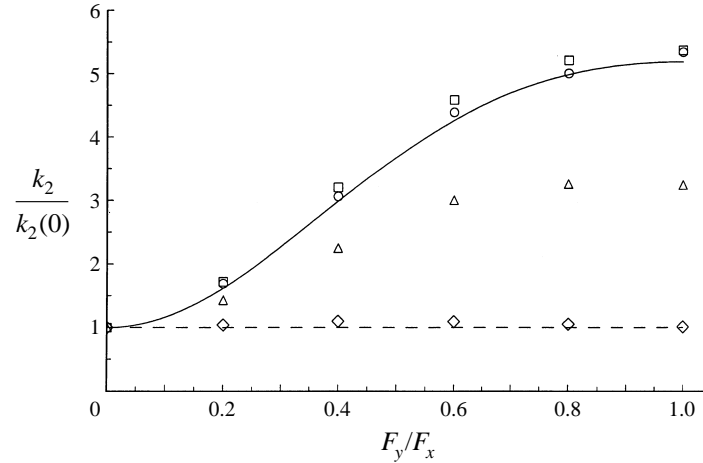


FIGURE 6. The coefficient k_2 defined in (3) is plotted as a function of F_y/F_x ; k_2 is normalized by its value at $F_y/F_x = 0$ in order to emphasize the variation of the inertially induced drag with the orientation of the force. The computational results are indicated by \circ ($\phi = 0.052$), \square ($\phi = 0.099$), \triangle ($\phi = 0.20$), and \diamond ($\phi = 0.40$). The solid line is the Oseen theory for dilute arrays and the dashed line the lubrication analysis for dense arrays.

By performing the sum for several values of q_m it was then possible to extrapolate to $q_m = \infty$. The result for the coefficient k_2 is

$$k_2 \phi = \frac{0.0286}{b^2} - \frac{0.0348}{b^3} + \frac{0.0146}{b^4}. \quad (32)$$

Equation (32) is plotted as the solid line at low volume fractions in figure 3. To obtain a better view of the comparison between the dilute theories and the computational results, we have plotted $k_2 \phi$ as a function of $[\ln(1/\phi)]^{-1}$ in figure 5. The theoretical results become accurate only for highly rarefied arrays. The computational results are in fair agreement with the Navier–Stokes theory for $[\ln(1/\phi)]^{-1} < 0.2$, corresponding to volume fractions less than about 0.005. The Oseen theory is only accurate at extremely small ϕ ; it deviates from the Navier–Stokes theory by 30% even at $[\ln(1/\phi)]^{-1} = 0.1$ or $\phi = 5 \times 10^{-5}$.

3.1.4. Numerical results for off-axis flows

Because the fluid inertia introduces nonlinearities into the equations of motion, the effect of inertia on the drag (as measured by k_2 , for example) is not independent of the orientation of the flow relative to the axes of the array. Figure 6 is a plot of k_2 normalized by its value for on-axis flow as a function of the ratio of the components of the drag (or pressure drop). As noted earlier, the lubrication theory (dashed line) predicts that k_2 is independent of F_y/F_x and this prediction is confirmed by the computational results for $\phi = 0.40$ (diamonds). As the volume fraction is decreased to $\phi = 0.20$ (triangles), k_2 begins to increase with F_y/F_x indicating that the drag is larger for off-axis flows. In the dilute arrays with $\phi = 0.099$ (squares) and $\phi = 0.052$ (circles), the variation of the drag reduces to that predicted by the Oseen theory (solid line). It is interesting to note that the Oseen theory provides excellent predictions of the angular variation of the drag for arrays as concentrated as $\phi = 0.1$, whereas it does not accurately predict the absolute value of the drag until the volume fraction is much smaller ($\phi \approx 10^{-4}$).

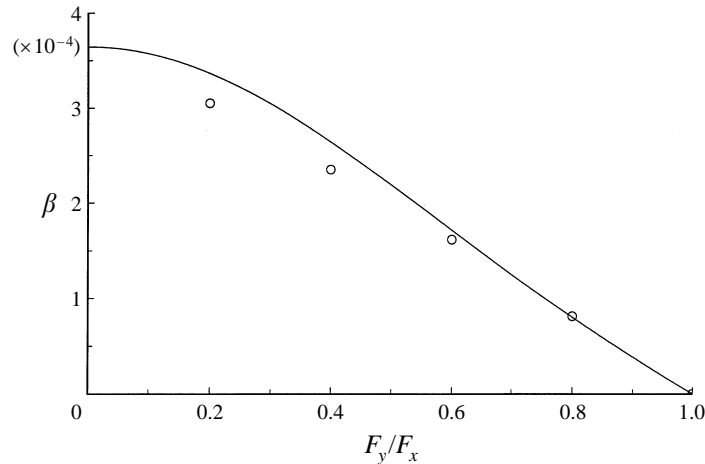


FIGURE 7. The coefficient β defined in (15) is plotted as a function of the ratio F_y/F_x of the components of the force: \diamond , results of computations with $\phi = 0.403$; solid line is lubrication theory (15).

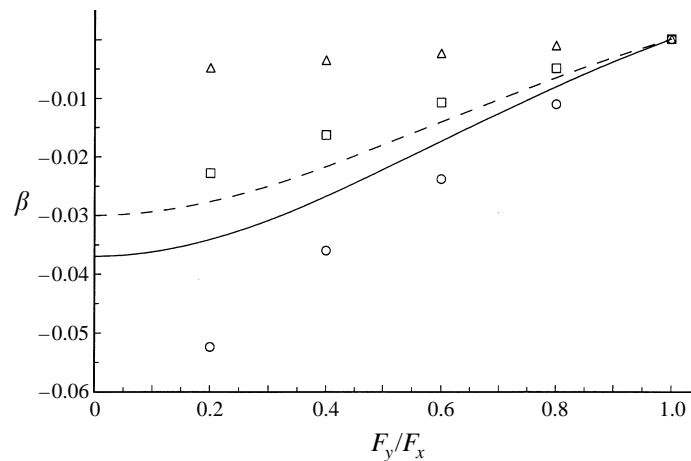


FIGURE 8. The coefficient β defined in (15) is plotted as a function of F_y/F_x . The symbols are computational results for $\phi = 0.052$ (\circ), 0.099 (\square), and 0.20 (\triangle). The solid and dashed lines are the Oseen theory for $\phi = 0.052$ and 0.099 , respectively.

At zero Reynolds number, the direction of the mean flow coincides with the direction of the drag (or pressure gradient) as a result of the principle of linear superposition. As noted in our discussion of the lubrication analysis, inertial effects lead to a difference between the angles that the flow and the force make with the axis of the array as expressed in (14). The lubrication analysis predicts a positive value of the coefficient β , indicating that the flow makes a larger angle with the primary axis of the array than does the force. Thus, the flow shifts in such a way as to make better use of the channels oriented in the y -direction as well as those oriented in the x -direction. The predictions of the lubrication analysis are compared with the numerical simulations for $\phi = 0.40$ in figure 7.

The value of β is negative at smaller values of ϕ as shown in figure 8, indicating that the mean velocity is more nearly aligned with the symmetry axis than is the pressure gradient. This may result from the fact that one cylinder can more effectively draft in the wake of its nearest neighbour when the flow is aligned with the primary axis of

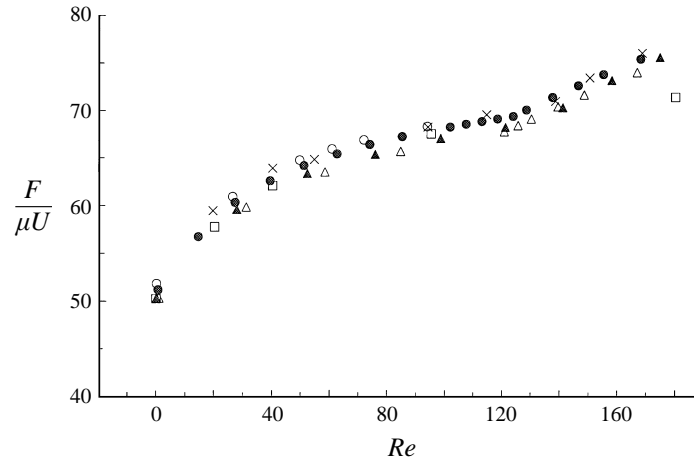


FIGURE 9. The drag for on-axis flow in a square array of cylinders with $\phi = 0.20$ is plotted as a function of the Reynolds number: \circ , \bullet , \triangle , \blacktriangle , are our simulations with $a = 4.8, 9.8, 14.8,$ and 19.8 , respectively; \square , finite element results of Edwards *et al.* (1990); \times , finite element solutions of Ghaddar (1995).

symmetry. A theoretical prediction for β based on the Oseen theory can be obtained easily by solving (23) and it is given by

$$\beta = \frac{\pi}{4\phi b} \left(\frac{(\mathbf{A}_0 \cdot \mathbf{V})_x}{V_x} - \frac{(\mathbf{A}_0 \cdot \mathbf{V})_y}{V_y} \right). \quad (33)$$

The theoretical results for $\phi = 0.052$ and 0.099 are plotted as the solid and dashed lines in figure 8. The theory predicts the correct qualitative trends, indicating that β is negative and that it becomes increasingly negative as the pressure gradients becomes aligned with the symmetry axis and as the volume fraction is decreased. However, the quantitative agreement is not good at these moderately small values of ϕ .

3.2. Moderate Reynolds numbers

The previous subsection emphasized the relationship between the mean velocity and drag at asymptotically low Reynolds numbers, for which theoretical analysis is possible. In this section, the lattice-Boltzmann computations will be used to explore this relationship at higher Reynolds numbers. Figure 9 gives the drag as a function of the Reynolds number for on-axis flow in a simple square array with $\phi = 0.2$. As the Reynolds number is increased from 0 to 180, $F/(\mu U)$ exhibits a modest increase of about 40%. The open and filled circles and the open and filled triangles indicate lattice-Boltzmann calculations with 10, 20, 30 and 40 grid spacings across the gap between particles, respectively. The squares are a finite element calculation by Edwards *et al.* (1990). There is a good agreement between the lattice-Boltzmann and finite element simulations for $Re < 100$. At higher Re , the flow becomes unsteady in our simulations whereas Edwards *et al.*'s computation sought only steady solutions. The drag versus Reynolds number plot exhibits an increase in slope after the onset of unsteadiness that is not seen in Edwards *et al.*'s solution. However, it has been observed in the finite element solutions of Ghaddar (\times) which solve the time-dependent Navier–Stokes equations. At $Re = 0$, the computation results are close to the prediction of $F/\mu U = 51.5$ obtained from a multipole solution of the Stokes equations (Sangani & Acrivos 1982). Figure 9 validates the lattice-Boltzmann code at finite Re by indicating that it

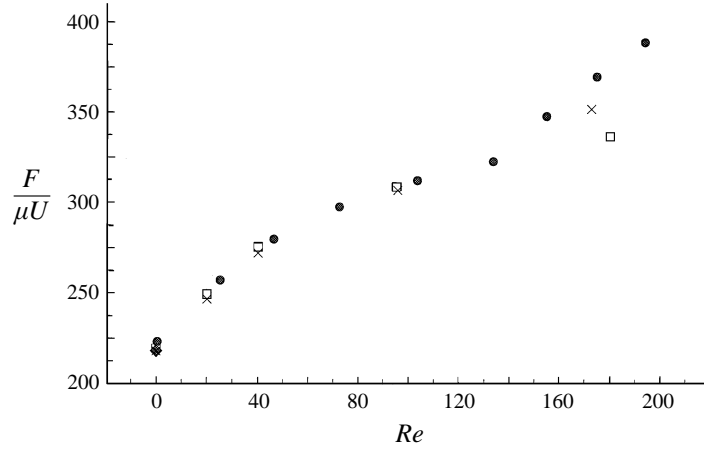


FIGURE 10. The drag for on-axis flow in a square array of cylinders with $\phi = 0.40$ is plotted as a function of the Reynolds number: \bullet , our simulations with $a = 25.8$; \square , steady-state finite element simulations (Edwards *et al.* 1990); \times , finite element solutions of the time-dependent Navier–Stokes equations (Ghaddar 1995); \blacklozenge , at $Re = 0$ is the multipole solution of Sangani & Acrivos (1982).

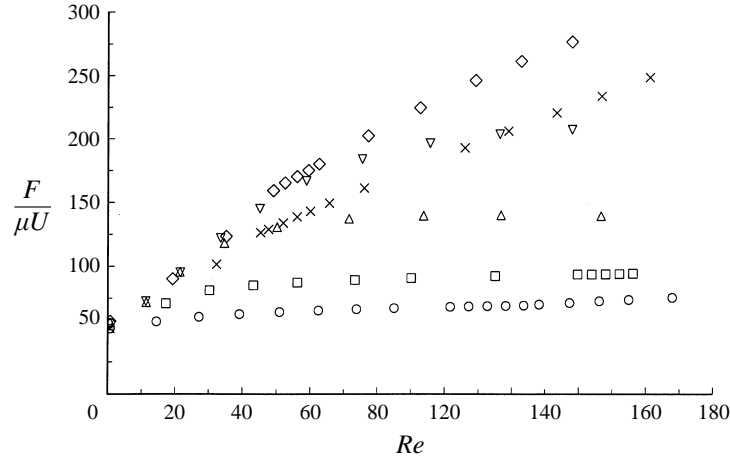


FIGURE 11. The drag on a cylinder, $F/\mu U$, in a square array with $\phi = 0.20$ is plotted as a function of Reynolds number for $F_y/F_x = 0$ (\circ), 0.2 (\square), 0.4 (\triangle), 0.6 (∇), 0.8 (\diamond), and 1 (\times). The radius is $a = 9.8$. In cases where the flow is unsteady F and U are the time-averaged force and mean velocity.

reproduces results obtained by other numerical methods and that the results are insensitive to the ratio of sphere radius to grid spacing, a , for sufficiently large values of a .

Figure 10 presents results for on-axis flow with $\phi = 0.40$. Again the agreement with both finite element solutions is good for $Re < 150$. At larger Re , the flow becomes unsteady and our lattice-Boltzmann simulations are in good agreement with Ghaddar's finite element solution of the time-dependent Navier–Stokes equations. At $Re = 0$, the lattice-Boltzmann drag, $F/\mu U = 223$, is comparable with that obtained from the multipole solution by Sangani & Acrivos (1982), i.e. $F/\mu U = 218$.

The nature of the fluid flow and the pressure drop/flow rate relationship in a square array at finite Re is strongly dependent on the angle that the pressure gradient makes with the axis of symmetry for the array. For example, figure 11 presents $F/\mu U$ as a

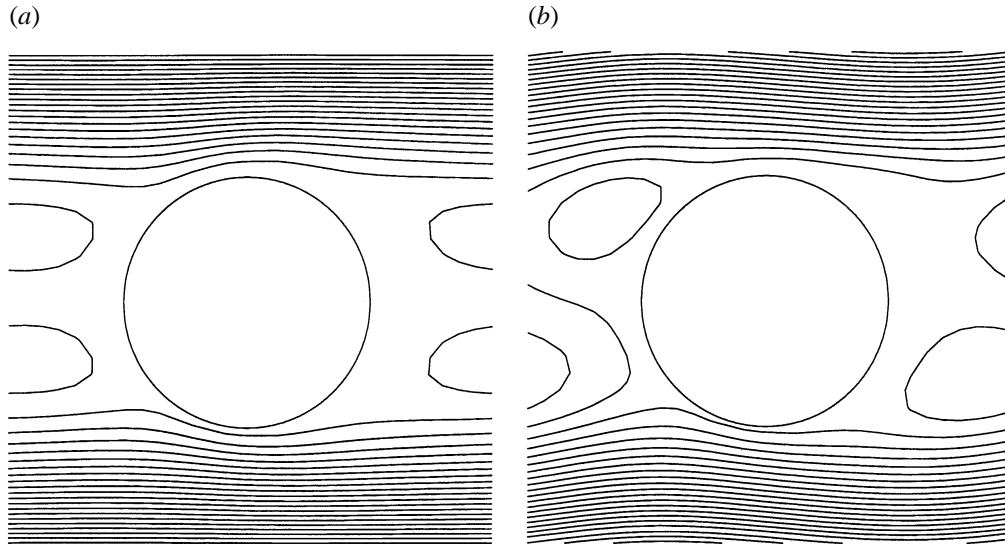


FIGURE 12. Streamlines for flow parallel to the axis of symmetry of a square array with $\phi = 0.20$ at $Re = 58.2$ (a) and 166.6 (b). The flow at $Re = 166.6$ is unsteady with $St = 0.64$, $\Delta\theta = 1.5$, and $\Delta U/U = 2.1 \times 10^{-4}$.

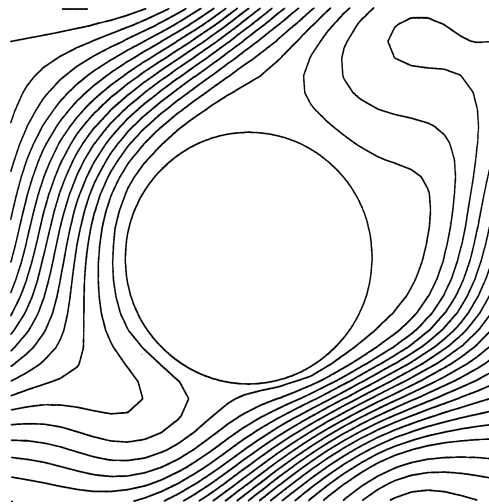


FIGURE 13. Streamlines for flow at a 45° angle to the primary axis of a square array with $\phi = 0.20$ and $Re = 61.5$. The flow is unsteady with $St = 0.74$, $\Delta\theta = 2.3$, and $\Delta U/U = 2.1 \times 10^{-3}$.

function of the Reynolds number for several orientations of the pressure gradient. As noted earlier, the drag for on-axis flow (circles) rises only modestly with Re . In contrast, the drag is a highly nonlinear function of the flow rate when the pressure gradient and mean velocity are directed at 45° to the axis of the array (\times)[†]. The origin of these vastly different behaviours may be discerned by examining the streamlines at $Re \approx 60$ (figures 12a and 13). For on-axis flow (figure 12a) the recirculating wake

[†] Our drag for $F_y/F_x = 1$ and $Re = 60$, $F/\mu U = 143$, is considerably larger than the value, $F/\mu U = 91$, reported by Edwards *et al.* (1990). This discrepancy may be attributed to the fact that Edwards *et al.*'s results are for steady flow, whereas we obtain an unsteady solution at this Re . To validate our code for off-axis flow, $F_y/F_x = 1$, we compared our result for $Re = 26.6$, $F/\mu U = 92.1$, with a spectral solution (Yusof 1996) which gave $F/\mu U = 91.8$ at $Re = 26.7$.

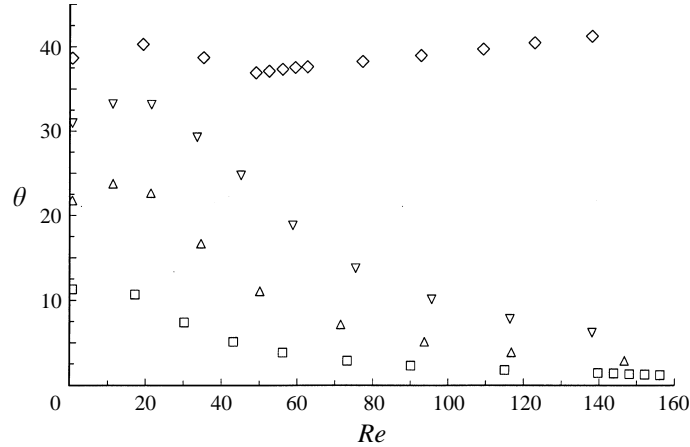


FIGURE 14. The angle that the mean velocity makes with the x -axis is plotted as a function of Reynolds number for a square array with $\phi = 0.20$ and $a = 9.8$. In cases where the flow is unsteady, the time average of θ is given. The symbols are as defined in figure 11.

behind one cylinder is able to bridge the gap to the next cylinder. Since the pressure variation within this wake is small and the wake comprises nearly equal parts of the front and rear of the cylinder, the form drag is nearly zero. Thus, the drag for on-axis flow is primarily a viscous stress arising from the non-recirculating flow and this drag is nearly proportional to μU . When the pressure gradient is at the 45° orientation, the wake behind the cylinder becomes unsteady before it is able to bridge the larger ($\sqrt{2}H$) distance to the next cylinder. At $Re \approx 60$, the flow is unsteady with vortices shed alternately from either side of the cylinder as may be seen in figure 13. This leads to an asymmetric pressure distribution and a substantial form drag, so that the drag per unit length is nearly proportional to $\rho U^2 a$.

At zero Reynolds number, the mean velocity of the fluid is always parallel to the drag. However, at higher Re , the mean velocity can have a different orientation from the drag when F_y/F_x is intermediate between 0 and 1. This is illustrated in figure 14 where the angle θ that the mean velocity makes with the x -axis is plotted as a function of Reynolds number for $F_y/F_x = 0.2$ (squares), 0.4 (upward triangles), 0.6 (downward triangles), and 0.8 (diamonds). For the smaller values of the ratio F_y/F_x , the flow angle θ shows a very slight initial increase with Re and then decreases dramatically, so that the mean flow is nearly aligned with the x -axis for $Re > 100$. This flow alignment allows a wake spanning the distance between two neighbouring cylinders to form. This may be seen in figure 15 which shows the streamlines for $F_y/F_x = 0.4$ and $Re = 60.6$. Although θ is only 4.6° , the slight asymmetry of the wake and the larger value of the x -velocity at y -positions smaller than the cylinder's centre produce a sufficient value of F_y to maintain the angle of the force with the x -axis at $\theta_f = 21.8^\circ$. By comparing figures 11 and 14, it can be seen that the force increases with Re initially for all the off-axis flows. However, for $F_y/F_x = 0.2, 0.4$ and 0.6 , the non-dimensional force achieves a nearly steady value after the flow becomes nearly aligned with the x -axis ($\theta \rightarrow 0$).

The behaviour for $F_y/F_x = 0.8$ is distinct from that at the other forcing orientations. The flow angle θ initially increases and decreases for $Re < 50$ in a manner similar to the other angles. However, at $Re = 50$, the flow becomes unsteady. As Re is further increased, the mean flow becomes increasingly aligned with the 45° direction.

Thus, at high Reynolds numbers, it is very difficult to drive a fluid flow through a square array at any orientation that is not parallel to one of the primary axes of

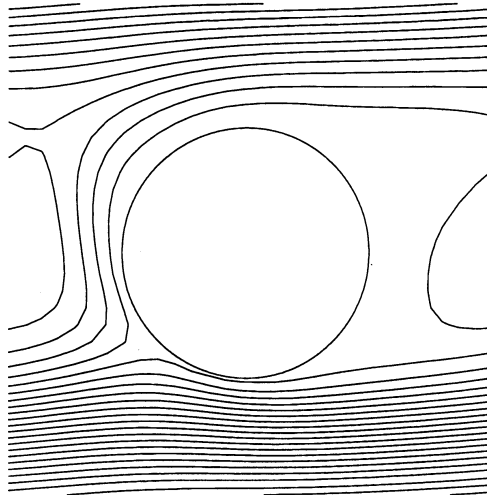


FIGURE 15. Streamlines for a pressure drop at an acute angle to the symmetry axis of a square array with $\phi = 0.20$, $F_y/F_x = 0.4$, $Re = 60.6$ and the angle between the flow and the primary axis is $\theta = 4.6^\circ$.

symmetry. There is a small domain of attraction for flows at a 45° angle to the primary axis, but most orientations of the pressure gradient lead to flows nearly aligned with one of the primary axes.

The flow past an isolated cylinder becomes unsteady at $Re = 49$ and the period of the oscillation may be characterized by a Strouhal number, $St = 2a/(UT)$, where T is the period of oscillation (Williamson 1996). The Strouhal number increases slowly with Re from a value of 0.12 at the onset of unsteady flow to 0.18 at $Re = 160$. We may therefore expect to observe unsteady flows in the range of Reynolds numbers studied here. In a periodic array, the transition to unsteady flow and the nature of the oscillations are strongly dependent on the orientation of the force. The Strouhal number and amplitude of the oscillations are given in table 1 for the cases in which oscillatory flow was observed. For $F_y/F_x = 1$ and 0.8 we observed a transition at Reynolds numbers quite close to the critical Re for an isolated cylinder, i.e. $Re \approx 46$ and 50, respectively. However, the Strouhal numbers at onset, $St = 0.74$ for $F_y/F_x = 1$ and $St = 0.70$ for $F_y/F_x = 0.8$, are considerably larger than for the unbounded flow. The higher frequency of oscillation in the array of cylinders may be attributed to the confinement of the flow by neighbouring cylinders leading to smaller vortices which are shed more frequently.

At the intermediate drag orientations $F_y/F_x = 0.6$, 0.4 and 0.2, we did not observe any unsteady flows. However, when the pressure gradient is aligned with the primary axis of symmetry, the flow becomes unsteady at a relatively large Reynolds number, $Re \approx 125$.[†] The amplitude of the oscillations for on-axis flow is quite small and the oscillation simply consists of a wave passing along the wake. This leads to a small form drag that accounts for the increase in the slope of the drag versus Re plot in figure 9.

[†] Ghaddar reported a transition to unsteady flow occurring between $Re = 138$ and 150. However, for $a = 9.8$, we obtained steady flow at $Re = 123.6$ and unsteady at $Re = 128.2$, and upon refining the grid (using $a = 14.8$) the transition was in the range $Re = 120.5$ – 125.3 . The amplitude of the oscillation is very small near onset. Also, if one starts from zero velocity, it takes a long time for numerical errors to break the symmetry and initiate the oscillation. For this reason we introduced some asymmetry in the initial conditions.

F_y/F_x	Re	$F/\mu U$	St	θ	$\Delta\theta$	$\Delta U/U$
1	45.3	126.3	Steady	45	—	—
	47.6	128.7	0.74	45	1.3	7.3×10^{-4}
	51.9	133.8	0.74	45	2.0	1.1×10^{-3}
	56.0	138.5	0.74	45	2.4	1.5×10^{-3}
	60.0	143.0	0.74	45	2.8	2.0×10^{-3}
	65.6	149.4	0.74	45	3.1	2.7×10^{-3}
	76.1	161.1	0.74	45	3.6	4.9×10^{-3}
	105.9	192.7	0.75	45	4.3	6.1×10^{-3}
	119.0	206.0	0.75	45	4.5	6.9×10^{-3}
	133.4	220.3	0.76	45	4.6	7.7×10^{-3}
	146.8	233.6	0.76	45	4.7	8.6×10^{-3}
	161.2	248.3	0.77	45	4.8	9.5×10^{-3}
	0.8	49.0	159.2	Steady	—	—
52.5		165.2	0.71	37.0	1.2	3.2×10^{-3}
56.0		170.2	0.72	37.3	1.8	4.4×10^{-3}
59.4		175.1	0.72	37.5	2.2	5.0×10^{-3}
62.6		180.0	0.72	37.6	2.5	6.2×10^{-3}
77.2		202.1	0.73	38.2	3.3	7.7×10^{-3}
92.7		224.5	0.74	38.9	3.6	8.2×10^{-3}
109.2		246.1	0.77	39.7	3.8	8.0×10^{-3}
122.8		261.1	0.77	40.4	3.9	7.7×10^{-3}
138.0		276.4	0.77	41.2	4.0	9.6×10^{-3}
0	123.6	69.4	Steady	0	—	—
	128.2	70.1	0.63	0	0.56	2.3×10^{-5}
	137.3	71.4	0.63	0	0.89	5.5×10^{-5}
	146.2	72.6	0.64	0	1.1	1.0×10^{-4}
	154.9	73.8	0.64	0	1.3	1.5×10^{-4}
	167.8	75.4	0.64	0	1.4	2.1×10^{-4}

TABLE 1. Data for unsteady flows in square arrays with $\phi = 0.2$. The values of Re , $F/\mu U$, and θ are time averaged. $\Delta\theta$ is the amplitude of the oscillations in θ , ΔU is the amplitude of the oscillation of the spatially averaged velocity, and U is the spatially and temporally averaged velocity.

To test the accuracy of the unsteady flow solutions, we repeated the highest Reynolds number flow with a 45° orientation using a larger cylinder, $a = 14.8$. This resulted in only a 2% change in the Strouhal number. We also performed a simulation with four periodically arranged cylinders in the unit cell. The flow did not exhibit oscillations with a spatial wavelength twice that of the array. Bittleston (1986) observed variations in the flow field in different unit cells in physical experiments at sufficiently high Reynolds numbers. However, it is not clear whether the variations in the experiments resulted because the flow was not fully developed; the array was only ten cylinders long and eight cylinders wide.

The variation of the drag with Reynolds number for off-axis flows in a more concentrated periodic array ($\phi = 0.40$) is plotted in figure 16. The angle between the mean velocity and the primary axis of the array is plotted in figure 17. As in the case of the more dilute array (cf. figure 14), the drag increases much more rapidly when $F_y/F_x = 1$ or 0.8 than when the pressure gradient is along the axis of symmetry ($F_y/F_x = 0$). However, the behaviour at intermediate orientations is different from that observed previously. At $\phi = 0.20$, the drag at the intermediate orientations ($F_y/F_x = 0.2, 0.4, \text{ and } 0.6$) levelled off as the Reynolds number was increased and the mean velocity became increasingly aligned with the primary axis (cf. figure 12). In the more concentrated array, the flow angle θ increases rapidly as Re is increased from $Re = 0$.

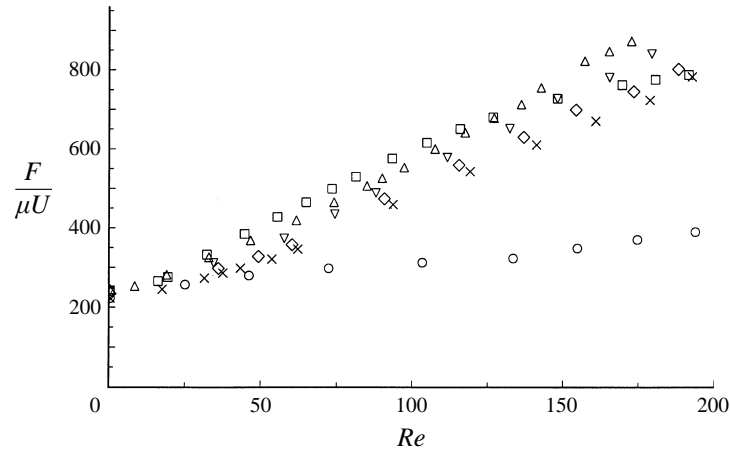


FIGURE 16. The drag on a cylinder, $F/\mu U$, in a square array with $\phi = 0.40$ is plotted as a function of Reynolds number for $F_y/F_x = 0$ (\circ), 0.2 (\square), 0.4 (\triangle), 0.6 (∇), 0.8 (\diamond), and 1 (\times). The radius is $a = 25.8$. In cases where the flow is unsteady F and U are the time-averaged force and mean velocity.

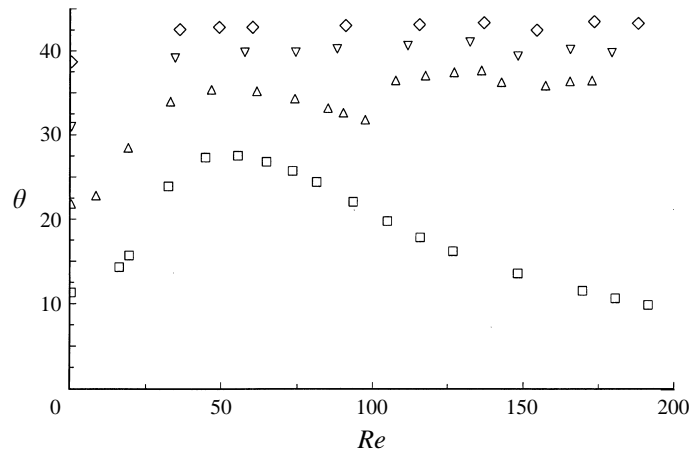


FIGURE 17. The angle that the mean velocity makes with the x -axis is plotted as a function of Reynolds number for a square array with $\phi = 0.40$ and $a = 25.8$. In cases where the flow is unsteady, the time average of θ is given. The symbols are as defined in figure 16.

At $F_y/F_x = 0.2$, the angle passes through a maximum and the flow eventually begins to align with the symmetry axis. As a result, the drag for this case finally begins to level off at $Re \approx 150$. At $F_y/F_x = 0.4$, θ first increases with Re , then passes through a maximum and begins to decrease. However, at $Re \approx 100$ the flow becomes unsteady and begins to oscillate close to the 45° orientation. For $F_y/F_x = 0.4, 0.6$, and 0.8 , $\theta \rightarrow 45^\circ$ at high Reynolds numbers. At these orientations, the drag is uniformly higher than that for $F_y/F_x = 1$, i.e. $\theta_F = 45^\circ$.

The dynamics of the flows observed in the array with $\phi = 0.40$ and summarized in table 2 are more complex than those in the more dilute array. When the forcing is along the axis of symmetry, we observe a simple transition to time-oscillatory flow at $Re \approx 140$. For $F_y/F_x = 0.2$, the flow remains steady for all the Reynolds numbers studied. However, when the forcing ratio is further increased to $F_y/F_x = 0.4$ and 0.6 , the flow undergoes a transition to a simple oscillation at $Re \approx 100$ and 60 , respectively.

F_y/F_x	Re	Osc.	$F/\mu U$	St	θ	$\Delta\theta$	$\Delta U/U$
1	53.6	S	320.9	—	—	—	—
	62.1	P1	346.2	1.40	45	2.6	7.6×10^{-4}
	178.7	P1	721.9	1.40	45	5.3	1.0×10^{-2}
	179.5	P17	730.6	0.0831	45	7.7	2.6×10^{-2}
	180.9	P19	761.9	0.0748	45	8.1	2.9×10^{-2}
	182.3	P21	768.3	0.0680	45	8.4	3.1×10^{-2}
	192.6	P39	781.4	0.0374	45	9.1	4.5×10^{-2}
0.8	49.2	S	327.7	—	42.8	—	—
	60.2	P1	357.1	1.28	42.8	1.6	1.3×10^{-3}
	148.5	P1	666.0	1.38	43.2	5.3	8.3×10^{-3}
	154.2	P2	697.1	0.709	42.4	7.8	1.9×10^{-2}
	180.0	P1	764.4	1.40	43.4	5.1	1.1×10^{-2}
	183.1	P13	775.0	0.108	43.4	5.9	1.6×10^{-2}
	188.1	P17	800.1	0.0814	43.2	7.6	3.1×10^{-2}
	194.2	C	830.3	—	42.4	—	—
0.6	57.6	S	373.1	—	39.8	—	—
	74.3	P1	434.1	1.31	39.8	3.8	4.7×10^{-3}
	132.2	P1	650.5	1.37	41.0	5.3	9.1×10^{-3}
	141.5	P2	698.6	0.700	39.5	7.6	3.4×10^{-2}
	148.0	P4	726.4	0.352	39.3	8.4	4.3×10^{-2}
	149.5	P8	733.4	0.176	39.2	8.6	4.9×10^{-2}
	150.9	P16	740.9	0.0884	39.1	8.8	5.3×10^{-2}
	152.6	C	—	—	—	—	—
0.4	97.3	S	552.4	—	31.8	—	—
	107.5	P1	600.1	1.37	36.5	4.6	1.0×10^{-2}
	127.0	P1	677.2	1.38	37.4	4.9	1.1×10^{-2}
	136.0	P2	711.4	0.689	37.6	5.3	1.5×10^{-2}
	149.7	P4	789.9	0.355	35.8	6.7	3.9×10^{-2}
	155.6	C	—	—	—	—	—
0	133.3	S	322.5	—	0	—	—
	154.7	P1	347.5	1.19	0	1.6	2.7×10^{-3}

TABLE 2. Data for time oscillatory and chaotic flows in square arrays with $\phi = 0.4$. S denote steady; P1 a simple oscillation; P17, P19 etc. oscillations with 17, 19 etc. times the original period, and C chaotic.

This is followed by a sequence of period-doubling transitions leading eventually to chaotic fluctuations in the mean velocity at Reynolds numbers larger than about 155. Because of the asymmetry of the forcing, vortices are formed only on one side of the cylinder (the lower right-hand side in figure 18). These vortices then translate along the right-hand side of the cylinder and detach from the upper right corner. The period-doubling transition seems to occur at approximately the same Reynolds number at which a second vortex begins to form before the previous vortex has detached; the interaction of these vortices may result in the transition.

When the forcing is closer to the 45° orientation, i.e. $F_y/F_x = 0.8$ and 1, the flow becomes more symmetric about the diagonal and vortices can be formed from both sides of the diagonal. In addition to this change in the flow geometry, there is a change in the dynamic transitions. At $F_y/F_x = 1$, the original simple oscillation is replaced by oscillations with 17, 19, 21, 23, etc. times the original period as the Reynolds number is increased. An example of temporal oscillations of θ is shown in figure 19 for the P17 oscillation. The angle shows peaks of varying amplitude. The flow oscillates to alternating sides of the diagonal with a period equal to the original primary period of

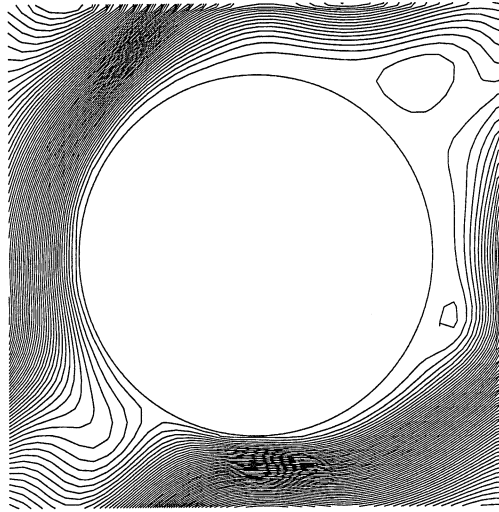


FIGURE 18. Streamlines for flow through a square array with $\phi = 0.40$, $F_y/F_x = 0.4$, and $Re = 142.6$ (corresponding to the P2 oscillation). At the instant at which these streamlines are taken, one vortex has reached the rear (top right) of the cylinder and a second is forming along the lower right-hand side.

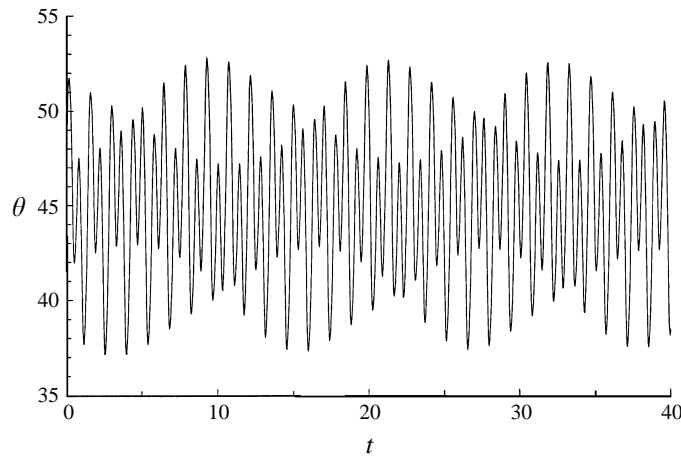


FIGURE 19. The temporal variation of the angle of the mean flow θ is plotted for the P17 oscillation at $Re = 186.8$ for an array with $\phi = 0.40$ and $F_y/F_x = 1$.

oscillation. However, approximately every fourth extremum of θ is larger than the others. Over the long P17 period, this large swing in the flow angle alternates between the two sides of the diagonal. For forcing along the 45° axis, no transition to chaotic motion has been observed. However, for $F_y/F_x = 0.8$, the flow becomes unsteady, passes through a period-doubling transition, returns to the P1 mode, and then passes through P13, P15, and P17 modes before becoming chaotic at $Re \approx 190$.

As in the case of the more dilute arrays, we tested the convergence of the computations by mesh refinement at the highest Re considered. We also confirmed that no spatial modes with wavelengths longer than the intercylinder spacing were observed when four cylinders were included in a unit cell. The flow past a single cylinder becomes three-dimensional at a Reynolds number of 195 (Williamson 1996). All of the simulations performed here for arrays of cylinders had Reynolds numbers smaller than

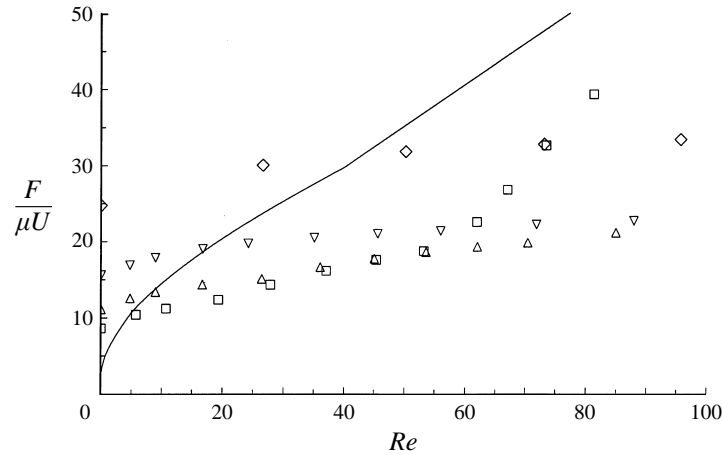


FIGURE 20. The drag for on-axis flow in dilute arrays; \diamond , ∇ , \triangle , \square , correspond to $\phi = 0.1$, 0.05 , 0.025 , and 0.0125 , respectively. The cylinder radius was 4.8 . The line is an empirical result (Clift, Grace & Weber 1978) for an isolated cylinder.

this critical value. However, to test for the possibility of three-dimensional flows, we performed a simulation which relaxed the assumption of two-dimensional symmetry. This test was performed at the highest Reynolds number, $Re = 172.6$, for which calculations were conducted at $\phi = 0.40$ and $F_y/F_x = 0.4$. Periodic boundary conditions were imposed in the direction parallel to the cylinder axis with a cell length equal to four times the cylinder diameter. This is large enough to include a three-dimensional mode of the type observed for the single cylinder (Williamson 1996). The simulation was conducted for a time $11 (2a/U)$, which is longer than the time required for the onset of unsteady two-dimensional flows. It was determined that the chaotically fluctuating flow remained two-dimensional.

The relatively modest increases in the drag with Reynolds number observed for on-axis flows in square arrays result from the drafting of each cylinder in the wake of its upstream neighbour. It is therefore interesting to determine how dilute an array can become before this drafting begins to lose its effectiveness. The drag in arrays with $\phi = 0.0125$, 0.025 , 0.05 , and 0.1 are plotted as a function of Reynolds number in figure 20. In these dilute arrays, drafting leads to a drag that is even smaller than that on an isolated cylinder (line) at the higher Reynolds numbers. The velocity field becomes unsteady at a Reynolds number that decreases with increasing dilution. The Reynolds number for the onset of unsteadiness is in the range $(57.0, 71.9)$ for $\phi = 0.05$, $(26.4, 36.0)$ for $\phi = 0.025$, and $(10.7, 19.4)$ for $\phi = 0.0125$. The Strouhal number at the onset of oscillations was $St \approx 1.0\phi^{1/2}$, consistent with computations of Bittleston (1986). These two observations suggest that the cylinder spacing H (instead of the particle diameter $2a$) is the length that characterizes the dynamics of dilute arrays. The onset Reynolds and Strouhal numbers based on H would be approximately constant at small volume fractions. At higher Reynolds numbers, $Re = (62.0, 70.5)$ at $\phi = 0.025$ and $Re = (45.4, 53.2)$ at $\phi = 0.0125$, the symmetry of the flow is broken and the time-average flow field is oriented off the axis of symmetry even though the pressure gradient coincides with this axis. When this occurs, the drag begins to increase more rapidly. The drag in the $\phi = 0.025$ array (upward triangles) begins to approach that in the more concentrated $\phi = 0.05$ array (downward triangles). The increase in the most dilute array ($\phi = 0.0125$ squares) is even more dramatic. The drag in this very dilute array

ϕ	N	N_c	F/U (\pm standard error)
0.20	4	100	45.1 ± 2.3
	16	20	42.0 ± 4.2
	32	20	39.6 ± 2.8
	64	10	43.7 ± 1.5
	128	5	40.1 ± 3.0
0.40	16	5	283 ± 13
	32	5	301 ± 35
	64	5	282 ± 32

TABLE 3. The mean drag in random arrays at $Re = 0$ for different values of the number of particles N in the unit cell.

a	Re	$F/\mu U$
13.8	0.0493	291.8
—	45.2	508.5
27.8	0.0468	307.2
—	43.6	527.4

TABLE 4. The mean drag in random arrays with $N = 4$ and $N_c = 5$ is given for two geometrically similar sets of configurations with different degrees of grid resolution.

grows until it is larger than even the $\phi = 0.1$ array (diamonds) and it begins to approach the result for an isolated cylinder (line).

4. Random arrays

4.1. Computational considerations

Random arrays of aligned cylinders can be simulated by including a large number, N , of cylinders within the unit cell. The positions of the centres of the cylinders were obtained using a standard Monte Carlo routine to simulate a hard-disk distribution. To obtain good statistical accuracy, it is necessary to average over an ensemble of N_c realizations of the hard-disk distribution. The mean drag is determined by averaging the drag obtained on all the cylinders in all of the various realizations.

To test for any possible dependence of the mean drag on N , we performed simulations at very small Reynolds numbers with $\phi = 0.20$, $a = 4.8$ and $\phi = 0.40$, $a = 13.8$ for several values of N . The mean drag and standard error (defined as the standard deviation among the members of the ensemble divided by $N_c^{1/2}$) are reported in table 3. The drag is independent of N to within the statistical accuracy of the calculations. For a large enough array, one would expect the statistical errors to be proportional to $(N_c N)^{-1/2}$. The computational costs are proportional to $N_c N$. A standard error of about 10% can be achieved using $N_c = 5$ and $N = 64$ and this choice was adopted for most of the subsequent computations. (The exceptions are the calculations for $\phi = 0.20$ where $N = 64$ and $N_c = 10$ and those at $\phi = 0.55$ and 0.60 for which $N = 32$ and $N_c = 10$. Sangani & Mo (1994) performed computations for the drag in random arrays of cylinders using a simulation of Stokes equations of motion based on multipole expansions for the velocity disturbance due to each cylinder and a novel method of including lubrication resistances. Using $N = 64$ and $N_c = 20$, they obtained $F/\mu U = 46.5$ and 278 at $\phi = 0.20$ and 0.40 , respectively. These results are consistent with the lattice-Boltzmann results listed in table 3.

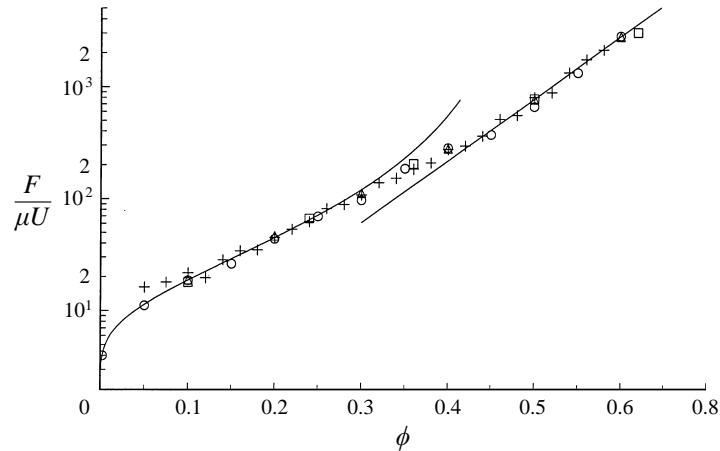


FIGURE 21. The mean drag in a random array of aligned cylinders at $Re = 0$ is plotted as a function of the volume fraction: \circ , our lattice-Boltzmann results; \triangle , multipole solutions of Stokes equations (Sangani & Mo 1994); $+$, finite element solutions (Ghaddar 1996); \square , lattice-Boltzmann results for arrays of octagons (Noble *et al.* 1997). The lines correspond to a solution of Brinkman's equations for low ϕ and a lubrication model for large ϕ .

4.2. Stokes flow

To test the convergence of the results for random arrays with grid refinement, we performed two sets of simulations with $N_c = 5$, $N = 4$, and $\phi \approx 0.4$. In the first set of simulations, the volume fraction and particle radius were $\phi = 0.404$ and $a = 13.8$, which corresponds to a mean spacing between neighbouring particles of 10. The linear dimensions of the unit cell and the components of the interparticle separation vectors were then precisely doubled and the particle radius was increased to $a = 27.8$. Since the cylinder radius could not be precisely doubled, the volume fraction of the larger array was $\phi = 0.409$. The results are summarized in table 4. The array of large particles had a 4–5% larger mean drag at $Re = 0$ and $Re = 45$ and this increase can be attributed primarily to the change in the volume fraction. Therefore, we concluded that a mean gap between the particles of 10 lattice spacings is sufficient to provide accurate results for the drag in random arrays with $Re \leq 45$. Subsequent calculations maintained this gap thickness with the exception of the dilute calculations $\phi = 0.05$ and 0.1 for which a gap of 16 lattice spacings was used.

Our results (circles) for the mean drag on random arrays of cylinders in the limit $Re \rightarrow 0$ are plotted as a function of volume fraction in figure 21. Our results are in good agreement with the Stokes flow solutions (triangles) of Sangani & Mo (1994), and the finite element solutions ($+$) of Ghaddar (1995). The statistical uncertainty of Ghaddar's results are largest at the smallest volume fractions. Whereas we maintained $N_c N = 320$ and Sangani & Mo maintained $N_c N = 1280$ for all the simulations, Ghaddar kept the ratio $H/a = 14$ constant and so his $N_c N$ varied from 720 at $\phi = 0.58$ to 60 at 0.05. We also show the lattice-Boltzmann results (squares) of Noble *et al.* (1997). Although these calculations are for octagonal cylinders, they yield essentially the same permeability as the arrays of circular cylinders to within the statistical accuracy of the results.

The lines in figure 21 correspond to two theoretical models. At low volume fractions, the drag in a random fixed bed can be determined from a solution of Brinkman's equations of motion, in which the effect of the particles is modelled as a body force

equal to the product of the fibre number density, the velocity, and a mean drag coefficient. This approach was used by Spielman & Goren (1968) to show that the drag on a dilute random array of aligned cylinders satisfies the implicit relationship

$$F/(\mu U) = 4\pi/A_s, \quad (34)$$

$$A_s = \frac{aK_1(a\kappa^{-1/2})}{\kappa^{1/2}K_0(a\kappa^{-1/2})} \frac{a^2}{2\kappa}, \quad (35)$$

where K_0 and K_1 are modified Bessel functions of the second kind and the permeability κ is related to the drag by

$$\kappa = \mu U a^2 / (4\phi F). \quad (36)$$

Howells (1974) showed that the relative errors in (34) are $O(1/\ln^2(1/\phi))$ in the limit of small volume fraction. However, it may be seen in figure 21 that the Brinkman prediction for the drag is much more robust than might be expected on the basis of the asymptotic analysis and it remains accurate for volume fractions as large as 0.3.

In §3, we found that the drag in a concentrated periodic array could be explained in terms of the lubrication resistance in the small gaps between the cylinders. A similar approach may be expected to work for random arrays. However, there is a distribution of gap thicknesses in a random array, which may be determined from the radial distribution function for the disks. Near contact, the radial distribution function may be approximated by

$$g(r) = \alpha_0 + \alpha_1(r-2) + \alpha_2(r-2)^2, \quad (37)$$

where r is the radial separation of the disks non-dimensionalized by a ,

$$\alpha_0 = \frac{16-7\phi}{16(1-\phi)^2}, \quad \alpha_1 = -14.2 + 78.3\phi - 119\phi^2 \quad (38)$$

and

$$\alpha_2 = 18.4 - 101\phi + 142\phi^2 \quad \text{for } \phi > 0.3. \quad (39)$$

The expression (38) for α_0 is obtained from a theoretical solution by Verlet & Levesque (1982), while α_1 and α_2 are obtained by fitting the first few points in Chae, Ree & Ree's (1969) simulations for $g(r)$ with a quadratic function. The simulations were performed for $\phi = 0.36, 0.45,$ and 0.54 and we have interpolated between these values. A characteristic minimum gap thickness may be obtained by integration:

$$2\pi n \int_2^{2+3\epsilon_m} g r \, dr = 1. \quad (40)$$

We approximate the drag in the random array as equivalent to that in a hexagonal array (derived by Sangani & Acrivos 1982) with a characteristic gap thickness ϵ_c , i.e.

$$\frac{F}{\mu U} = \frac{17\pi}{4\sqrt{2}\epsilon_c^{5/2}}, \quad (41)$$

where we choose $\epsilon_c = 1.19\epsilon_m$ in order to match the simulated drag value at $\phi = 0.6$. Thus, using one adjustable parameter, we obtain a lubrication theory that is in good agreement with the simulation results for $\phi \geq 0.4$.

4.3. Small (but finite) Reynolds number

Now let us consider the dependence of the drag on the Reynolds number. Although the standard error in the simulated mean drag is about 10%, we are able to obtain statistically significant results for very small changes in the drag with Reynolds

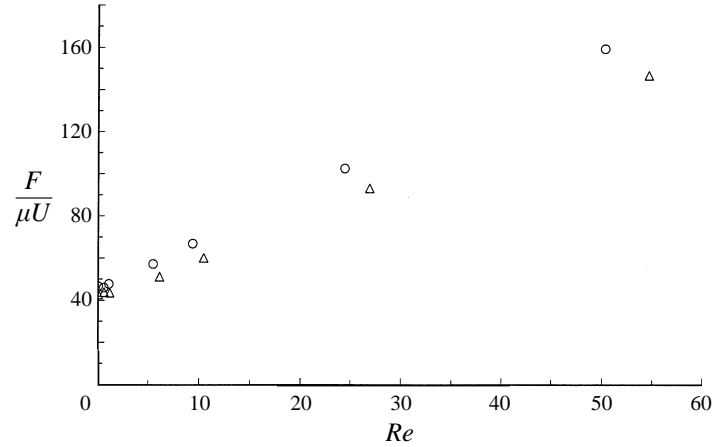


FIGURE 22. The mean drag coefficients for two sub-ensembles with $\phi = 0.20$, $a = 4.8$, $N_r = 5$ are plotted as functions of the Reynolds number.

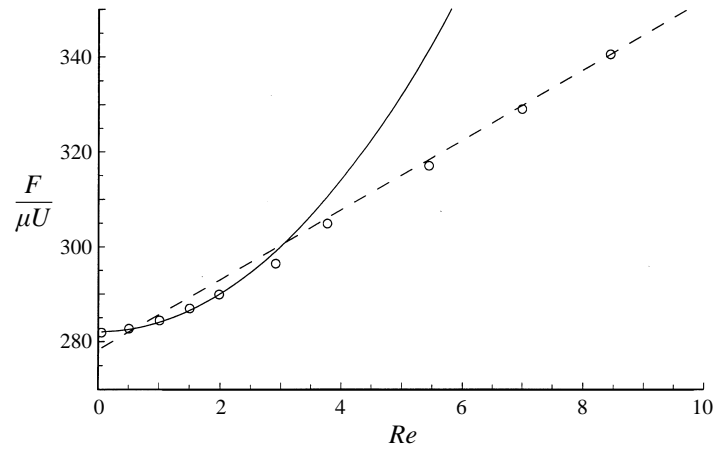


FIGURE 23. The mean drag in a random array with $\phi = 0.40$ and $a = 13.8$ is plotted as a function of the Reynolds number. The solid line is the low- Re asymptote (41) with $k_0 = 282.0$ and $k_2 = 2.01$ and the dashed line is the Ergun correlation (43) with $c_0 = 278.3$ and $c_1 = 7.36$.

number. This is possible because we use the same set of configurations at each of the Reynolds numbers. Thus, the primary effect of the statistical errors is a systematic shift in the drag versus Reynolds number curve as may be seen when we plot the results from two sub-ensembles with the same value of $\phi = 0.2$ in figure 22.

Mei & Auriault (1991) have shown that the initial increase in the mean drag with Reynolds number is quadratic:

$$F/(\mu U) = k_0 + k_2 Re^2 \quad \text{for } Re \ll 1. \quad (42)$$

However, the empirical relationship due to Ergun (1952) that has been very successful in describing experimental data on pressure drop in fixed beds is linear:

$$F/(\mu U) = c_0 + c_1 Re. \quad (43)$$

Our simulations confirm the validity of both of these expressions and show a transition from the quadratic low-Reynolds-number asymptotic behaviour to the linear moderate-Reynolds-number empirical scaling at $Re \approx 3$. This may be seen in figure 23, which presents results for $\phi = 0.4$.

Before examining further numerical evidence for the small (but finite)-Reynolds-number behaviour of the drag, we will develop a theoretical prediction for the drag in a dilute array. Kaneda (1986) used an ensemble-averaged-equation approach to determine the mean drag in a dilute random bed of spheres, when the Reynolds number, Re , based on the sphere diameter is small but the Reynolds number $R \equiv Re \kappa^{1/2}/(2a)$ based on the Brinkman screening length (or square root of the permeability) may be of order one. His analysis can easily be extended to the present two-dimensional flow problem. The approximations used by Kaneda to simplify the ensemble-averaged equations can still be applied in two dimensions, albeit with changes in the order of magnitude of the errors incurred.

The problem of determining the fluid velocity around a test cylinder in the random array may be solved using a singular perturbation method. The inner solution, valid within an $O(a)$ distance from the cylinder, is unaffected by inertia and the body force produced by the other cylinders and is given by (18).

The outer solution, valid at large $O(\kappa^{1/2}) = O(a(\ln(1-\phi)/\phi)^{1/2})$ distances, will be obtained by solving an approximate form of the conditional ensemble average of the Navier–Stokes equations, (4) and (5), with the centre of one cylinder held fixed, i.e.

$$\rho \nabla \cdot \langle \mathbf{u}\mathbf{u} \rangle_1 + \nabla \langle p \rangle_1 - \mu \nabla^2 \langle \mathbf{u} \rangle_1 - \langle \mathbf{f} \rangle_1 = \mathbf{F} \delta(\mathbf{x}), \quad (44)$$

$$\nabla \cdot \langle \mathbf{u} \rangle_1 = 0, \quad (45)$$

Here \mathbf{F} is the force per unit length that the test cylinder exerts on the fluid and \mathbf{f} is the force per unit volume that the remaining cylinders exert on the fluid. In (44), the effect of the test cylinder on the fluid velocity has been represented as a point force. This approximation leads to $O(a/\kappa^{1/2})$ relative errors at the large separations under consideration.

To leading order in small ϕ , the drag on a cylinder is determined solely by the length scale on which the fluid velocity disturbance produced by the cylinder begins to decay. As long as $R \leq O(1)$, this length scale will remain the Brinkman screening length, $\kappa^{1/2}$, and the relative change in the drag due to inertia will be small, $O(1/\ln(1/\phi))$. We will neglect this change when calculating the fluid velocity disturbance produced by the fibre using (44).

The force per unit volume, $\langle \mathbf{f} \rangle_1$, is small in a dilute array and only becomes important at large $O(\kappa^{1/2}) = O(a(\phi/\ln(1/\phi))^{-1/2})$ separations from the test cylinder where the viscous stress term $\mu \nabla^2 \langle \mathbf{u} \rangle_1$ is also small. At these large separations, $\langle \mathbf{f} \rangle_1$ can be approximated as the product of the fibre number density and the drag experienced by a fibre in a uniform velocity field of strength $\langle \mathbf{u} \rangle_1$. In addition, we can neglect the Reynolds-number dependence of $\langle \mathbf{f} \rangle_1$. Thus, with $O(1/\ln(1/\phi))$ relative errors,

$$\langle \mathbf{f} \rangle_1 \approx -(\mu/\kappa) \langle \mathbf{u} \rangle_1, \quad (46)$$

where κ is the Stokes flow permeability given by (36), (34) and (35).

The inertial term in (44) may be written in the form

$$\rho \nabla \cdot \langle \mathbf{u}\mathbf{u} \rangle_1 = \rho \mathbf{U} \cdot \nabla \langle \mathbf{u} \rangle_1 + \rho \langle \mathbf{u}' \rangle_1 \cdot \nabla \langle \mathbf{u} \rangle_1 + \rho \nabla \cdot \langle \mathbf{u}'' \mathbf{u}'' \rangle_1, \quad (47)$$

where $\mathbf{u}' = \mathbf{u} - \mathbf{U}$ and $\mathbf{u}'' = \mathbf{u}' - \langle \mathbf{u}' \rangle_1$. The fluid velocity disturbance $\langle \mathbf{u}' \rangle_1$ is $O(1/\ln(1/\phi))$ smaller than the mean velocity \mathbf{U} in the outer region so the second term on the right-hand side of (47) can be neglected. The spatially varying Reynolds stress produced by the test cylinder results from multiple reflections involving the test cylinder and one additional cylinder; it may be approximated as

$$\langle \mathbf{u}'' \mathbf{u}'' \rangle_1 \approx n \int d\mathbf{x}_2 \langle \mathbf{u}'' \rangle_2 \langle \mathbf{u}'' \rangle_2, \quad (48)$$

where \mathbf{x}_2 is the position of the second cylinder's centre. The velocity field due to multiple reflections is $\langle \mathbf{u}' \rangle_2 = O(U/(\ln(1/\phi))^2)$. The integral converges at the Brinkman screening length $\kappa^{1/2}$. Therefore, the spatially varying Reynolds stress can be determined to be $O(1/(\ln(1/\phi))^3)$ smaller than the first term on the right-hand side of (47) and it will be neglected.

Using the aforementioned approximations, the momentum equation reduces to a form that will be referred to as the Oseen–Brinkman equation:

$$\rho \mathbf{U} \cdot \nabla \langle \mathbf{u} \rangle_1 + \nabla \langle p \rangle_1 - \mu \nabla^2 \langle \mathbf{u} \rangle_1 + (\mu/\kappa) \langle \mathbf{u} \rangle_1 = \mathbf{F} \delta(\mathbf{x}). \quad (49)$$

Equations (45) and (49) constitute a linear set of equations for the conditionally averaged velocity and pressure. Solving these equations after taking a Fourier transform yields the following expression for the fluid velocity disturbance induced by the test cylinder:

$$\langle \hat{\mathbf{u}}' \rangle_1 = \hat{\mathbf{u}}_s + \hat{\mathbf{u}}_I, \quad (50)$$

where the fluid velocity disturbance in the absence of inertia is

$$\hat{\mathbf{u}}_s = \frac{\mathbf{F} \cdot (\mathbf{I} - \mathbf{Q}\mathbf{Q})}{\mu(2\pi q)^2 + \mu\kappa^{-1}} \quad (51)$$

and the change in the velocity due to inertia is

$$\hat{\mathbf{u}}_I = \frac{-\rho \mathbf{U} \cdot 2\pi i q \mathbf{F} \cdot (\mathbf{I} - \mathbf{Q}\mathbf{Q})}{[\mu(2\pi q)^2 + \mu\kappa^{-1}][\mu(2\pi q)^2 + \mu\kappa^{-1} + \rho \mathbf{U} \cdot 2\pi i q]}. \quad (52)$$

Evaluating the extra velocity disturbance due to inertia at the centre of the test cylinder gives

$$\mathbf{u}_I(\mathbf{x} = 0) = \int d\mathbf{q} \hat{\mathbf{u}}_I = -\frac{A_I \mathbf{F}}{4\pi\mu}, \quad (53)$$

where

$$A_I = -\frac{1}{2} + \left(\frac{2}{R^2} + \frac{1}{2}\right) \ln\left(1 + \frac{R^2}{4}\right). \quad (54)$$

Matching the outer solution derived above to the inner solution (18) gives rise to the following relationship between the drag on the cylinder and the mean velocity:

$$\frac{F}{\mu U} = \frac{4\pi}{A_S - A_I}. \quad (55)$$

Here A_S is the value of $4\pi\mu U/F$ under conditions of Stokes flow. The dilute analysis given above would yield the result that A_S is equal to the low-volume-fraction asymptote of (35), i.e. $A_S = \ln(1/\phi^{1/2})$. However, more accurate predictions for finite ϕ can be obtained by retaining the full implicit relations for A_S obtained by solving the Brinkman equation around a cylinder of finite radius, i.e. (35) and (36).

In the limit $R \ll 1$, (55) and (54) reduce to the form (42) expected for the regular perturbation to the drag at low Reynolds number with the coefficient controlling the first effects of inertia given by

$$k_2 = \frac{k_0}{256\phi}. \quad (56)$$

We have performed sequences of low-Reynolds-number simulations for several ϕ and obtained the coefficients in the asymptotic expression (42). The ratio $k_2\phi/k_0$ is

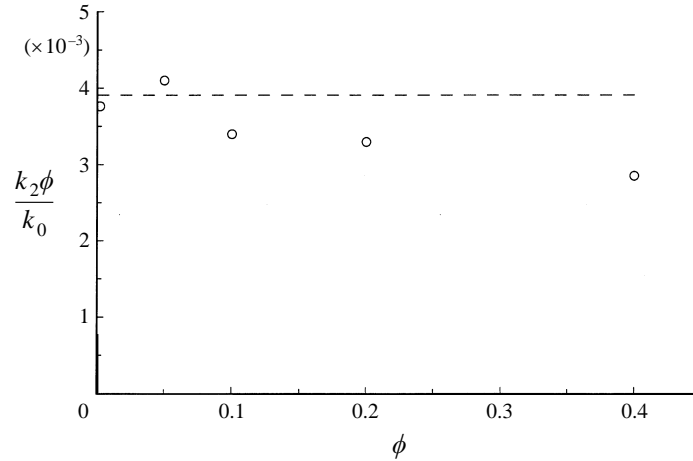


FIGURE 24. The ratio of coefficients, $k_2 \phi/k_0$, describing the first effects of inertia at low Reynolds number are plotted as a function of ϕ . The circles are simulation results and the dashed line is the result, $k_2 \phi/k_0 = 1/256$, obtained from the Oseen–Brinkman theory.

plotted versus ϕ in figure 24, comparing the simulations (circles) with the Oseen–Brinkman theory (dashed line). Although the theory is asymptotically valid only in the limit $\phi \rightarrow 0$, it can be seen that the Oseen–Brinkman expression for the first effects of inertia (56), like the Brinkman result for the drag in Stokes flow (34)–(36), is accurate even for moderate ϕ . In view of the similarities in the derivations of k_2 for dilute periodic and random arrays, it is surprising that the Oseen predictions for random arrays are much more accurate at moderate ϕ than those for periodic arrays. Both analyses neglect terms that are $O(1/\ln(1/\phi))$ as $\phi \rightarrow 0$. It is possible that there is a cancellation of errors in the random array analysis between the effects of the nonlinear inertial term and the Reynolds stress.

Equations (55) and (54) provide predictions for the drag that are valid when the Reynolds number, R , based on the Brinkman screening length is order one, as long as the Reynolds number, Re , based on the particle diameter is small. However, the usefulness of this $R = O(1)$ theory is limited, because the screening length only becomes appreciably larger than the cylinder diameter for very small values of volume fraction. In figure 25, we present the predictions of the Oseen–Brinkman theory for $\phi = 0.002$. The full theory (solid line) approaches the regular perturbation asymptote (dotted line) for $R \ll 1$. When $R \gg 1$, the inertial (Oseen) term dominates over the D’Arcy term in (49) and the full theory approaches the solution of Oseen’s equations for flow past a single cylinder (dashed line). We performed simulations for $\phi = 0.002$ with $a = 0.61$. The simulation results (circles) follow the finite- R theory (solid line) for a limited range $Re < 0.6$ after the full theory deviates from the small- R asymptote (dotted line). However, at larger Re , the simulations approach the empirical results for finite- Re flow past a single cylinder (dash-dot line), which deviates from the Oseen approximation at finite Re . Thus, it would be necessary to consider a still more permeable array to obtain an extended range of Reynolds numbers over which the Oseen–Brinkman theory describes the flow.

4.4. Moderate Reynolds numbers

We noted earlier that the mean drag in arrays with moderate values of ϕ exhibits a transition from a quadratic Re dependence at small Reynolds number to a linear dependence at higher Re , cf. figure 23. The linear relationship between drag and

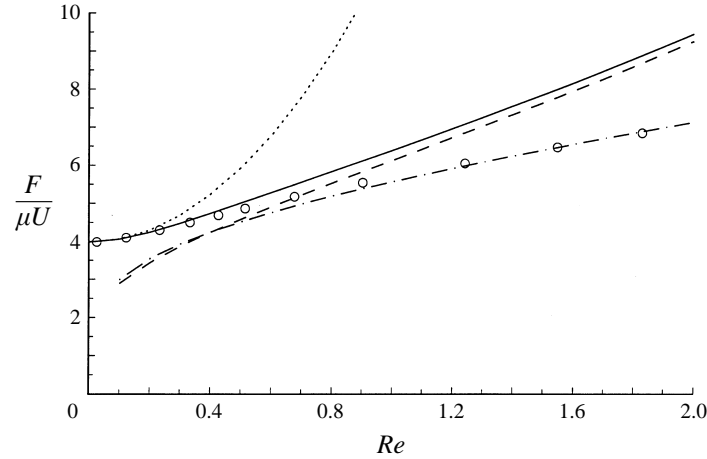


FIGURE 25. The mean drag in a random array with $\phi = 0.0020$ is plotted as a function of the Reynolds number: \circ , the simulations; —, the Oseen–Brinkman theory valid for $Re \ll 1$;, the asymptote for $Re(H/a) \ll 1$; ---, the Oseen result for a single cylinder; -·-·-, the empirical results (Clift *et al.* 1978) for a single cylinder valid at $0.1 < Re < 5$.

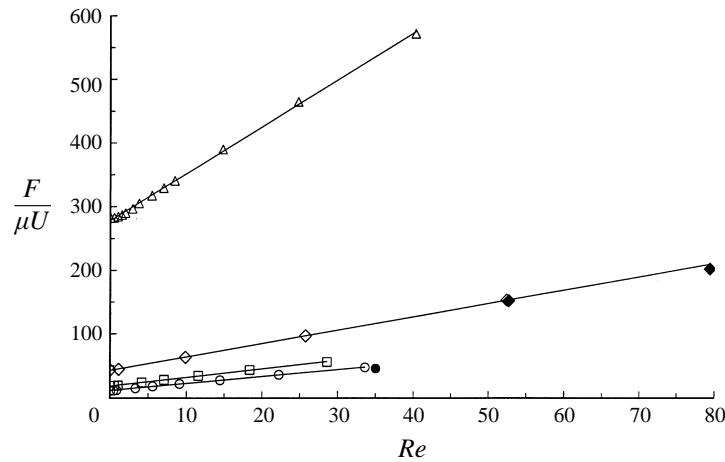


FIGURE 26. The mean drag is plotted as a function of Reynolds numbers for arrays with $\phi = 0.05$ (\circ), 0.1 (\square), 0.2 (\diamond), and 0.4 (\triangle); \diamond , \blacklozenge , $a = 4.8$ and 9.8 , respectively; \circ , \bullet , $a = 2.7$ and 4.8 , respectively.

Reynolds number at moderate values of the volume fraction and Reynolds number is quite robust as may be seen in figure 26, where simulation results for $\phi = 0.05, 0.1, 0.2$ and 0.4 are compared with the linear empirical relationship (43).[†]

Since the empirical relationship (43) provides a good description of the drag, we can use the ratio of the coefficients, c_1/c_0 , to characterize the Reynolds-number dependence of the drag for arrays with a wide variety of volume fractions. We performed a series of three simulations with Reynolds numbers in the range $0 < Re < 30$ for each volume fraction and obtained the coefficients from a linear regression. The ratio c_1/c_0 is plotted

[†] Some of the flows at the larger Reynolds numbers are unsteady. The oscillations in the mean velocity, however, are quite small. This is likely to be due to the fact that the vortex shedding from different cylinders in the random array is out of phase. The reported values of the drag represent time averages.

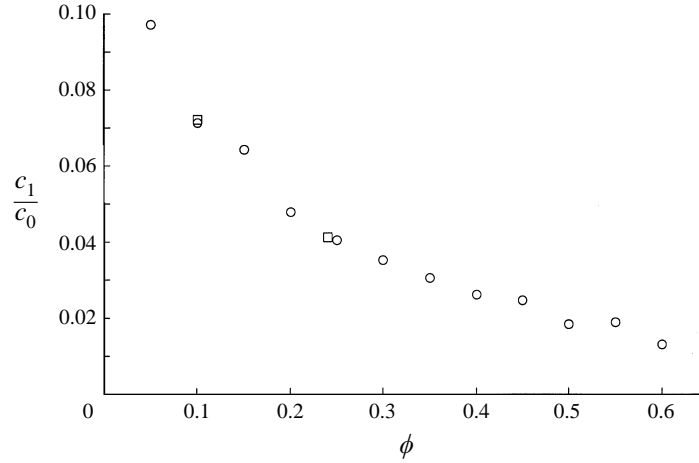


FIGURE 27. The ratios c_1/c_0 of the two coefficients obtained by fitting the Ergun empirical equations (43) to our simulation data (○) are plotted as a function of the volume fraction; □, the corresponding data for arrays of octagons (Noble *et al.* 1997).

as a function of volume fraction in figure 27. It can be seen that this ratio decreases monotonically with increasing volume fraction, indicating that inertial effects are weaker in more concentrated arrays.

We can rationalize this result by considering the relative importance of viscous effects and inertia in the limit as the volume fraction approaches maximum packing. It was noted earlier that the pressure drop required to overcome the viscous resistance to flow through the small gaps (of thickness $a\varepsilon$) between the cylinders is $O(\mu U/(a\varepsilon^{5/2}))$. When the inertia of the fluid is important, there is a pressure drop required to accelerate the fluid to the high velocity $u_g = O(U\varepsilon^{-1})$ it achieves in the gap. This pressure drop may be estimated using Bernoulli's equation to be $O(\rho U^2\varepsilon^{-2})$. The ratio of the inertial to the viscous pressure drop is $Re \varepsilon^{1/2}$, suggesting that c_1/c_0 will decrease as one approaches the maximum packing limit, i.e. as $\varepsilon \rightarrow 0$.

Noble *et al.* (1997) studied moderate-Reynolds-number flows through random arrays of octagonal cylinders. Their data for $\phi = 0.1$ at $Re = 5, 10$ and 15 show a linear dependence of the drag on Re , consistent with the present simulations and the Ergun relationship. Only two data points at moderate Re (5 and 10) were given for $\phi = 0.24$. Assuming that the Ergun relation applies at $\phi = 0.24$ as well as $\phi = 0.1$, the two squares in figure 26 can be obtained by fitting the data. Thus, the Ergun coefficients obtained from fitting Noble *et al.*'s low-to-moderate volume fraction data are in excellent agreement with those obtained in the present study. At the higher volume fraction, $\phi = 0.36$, Noble *et al.* (1997) observed an extended region of nonlinear Re -dependence for $F/\mu U$, extending to the highest Reynolds number ($Re = 32$) that they investigated. This behaviour may be contrasted with that illustrated in figure 23 where we observed a transition to a linear $F/\mu U$ versus Re behaviour at $Re \approx 5$. These comparisons indicate that the drag is insensitive to the small differences in shape between circles and octagons as long as the spacing between the particles is reasonably large. However, at higher concentrations, the gaps between circular particles are narrower and more tapered whereas the gaps between aligned octagons are wider (for the same ϕ) and relatively straight. The flow in the gaps between the octagons is closer to a unidirectional flow than that between the circles. Furthermore, the velocity in the gaps between the octagons is smaller than that in the narrower gaps between the circles.

For these reasons the inertial effects are weaker in the arrays of octagons, the transition to Ergun behaviour is delayed, and the drag is smaller than in the arrays of circles.

5. Conclusions

This paper has reported the results of lattice-Boltzmann simulations for the drag (or pressure drop) versus flow rate relationship in arrays of aligned cylinders at finite Reynolds numbers. These numerical calculations have been supplemented by theoretical calculations valid in the limit $Re \ll 1$. Both random arrays and periodic square arrays have been investigated.

The results for very small Reynolds numbers are consistent with those derived from solutions of Stokes equations of motion in periodic (Sangani & Acrivos 1982) and random (Sangani & Mo 1994) arrays. The initial increase in $F/(\mu U)$ with increasing Reynolds number is quadratic as predicted by Mei & Auriault (1991). We have developed analytical predictions for the coefficient of the quadratic term in the limits of small and large volume fraction. As the volume fraction in a square array approaches the close-packing limit, all of the fluid must flow through the small gap $a\epsilon$ between neighbouring cylinders and the pressure drop is controlled by the flow in this lubrication gap. Because of the early unidirectional nature of the flow in the gap, the effects of inertia are small and the coefficient of the quadratic term is proportional to ϵ .

The fluid velocity in a dilute square array can be obtained by a singular perturbation analysis based on a viscous-dominated inner region near the cylinder and an outer region whose size is comparable to the inter-fibre spacing. Inertia is important only in the outer region when the Reynolds number based on the cylinder diameter is small but the Reynolds number based on the fibre spacing is $O(1)$. A similar perturbation analysis can be performed on the ensemble-averaged equations of motion in a dilute random array. Inertial effects are strong in dilute periodic and random arrays, because the relevant Reynolds number is based on the largest length scale in the array, i.e. the inter-cylinder spacing in a periodic array and the Brinkman screening length in a random array. The idea that the Reynolds and Strouhal numbers based on the inter-fibre spacing are the most relevant parameters in dilute fibre beds was also suggested in our studies of dynamic transitions at higher Reynolds numbers.

Numerical simulations were performed for flows through square arrays of cylinders at Reynolds numbers up to 190 and a number of interesting phenomena were observed. The linearity of Stokes equations of motion requires that the pressure drop in a square array must be independent of the angle that the mean velocity makes with the array at $Re = 0$. However, at larger Reynolds numbers, a very strong anisotropy of the pressure drop versus flow rate relationship is observed. The pressure drop required to drive the flow along one of the principle axes of symmetry of the flow is much smaller than that required to drive off-axis flows. In addition, the direction of the mean velocity vector does not in general coincide with the direction of the pressure gradient.

As the flow rate in the simulations was increased, transitions to unsteady flow were observed. In some cases, the temporal variations of the mean velocity even become chaotic, while the fluid flow remains two-dimensional. The critical Reynolds numbers for the onset of unsteady flow, period doubling, and transition to chaos depend on the volume fraction and the orientation of the imposed pressure gradient. Even the nature of the dynamic transitions changes with the orientation of the pressure gradient. Period-doubling transitions were observed for pressure gradients near the primary axis

of the array, while transitions to odd multiples of the original period were found for pressure gradients along the diagonal of the array.

The permeability of a square array of cylinders under Stokes flow conditions increases monotonically with decreasing volume fraction. However, simulations for moderate-Reynolds-number on-axis flow through dilute square arrays indicate that the drag can actually be lower than that on an isolated cylinder as a result of the drafting of each cylinder in the wake of its predecessors in the same row.

Simulations were performed for flows through random arrays of cylinders with Reynolds numbers as high as 80. The ratio of the mean drag to the mean velocity, $F/\mu U$, exhibits a quadratic dependence on Re at small Reynolds numbers as already noted. However, for Reynolds numbers greater than about 5, there is a transition to a linear $F/\mu U$ versus Re behaviour of the form anticipated by the empirical Ergun equation. The drag versus flow rate relationship for a large range of volume fractions was characterized by fitting the results of the simulations to the Ergun equation. The ratio, c_1/c_0 , of the inertial to the viscous coefficient decreases monotonically with increasing volume fraction. Near the close-packing limit, the pressure drop is controlled by the viscous pressure gradient required to drive flow through the narrow lubrication gaps between neighbouring cylinders.

This work was supported by the National Science Foundation through grant number CTS-9526149. The computations were performed on the facilities of the Cornell Theory Center.

REFERENCES

- BITTLESTON, S. H. 1986 Flows past arrays of cylinders. PhD thesis, Bristol University.
- BRADY, J. F. & BOSSIS, G. 1988 Stokesian Dynamics. *Ann. Rev. Fluid Mech.* **20**, 111.
- BRINKMAN, H. C. 1947 A calculation of the viscous force exerted by a flow fluid on a dense swarm of particles. *Appl. Sci. Res. A* **1**, 27.
- CHAE, D. G., REE, F. H. & REE, T. 1969 Radial distribution functions and equation of state of the hard-disk fluid. *J. Chem Phys.* **50**, 1581.
- CHAPMAN, S. & COWLING, T. G. 1970 *The Mathematical Theory of Non-Uniform Gases*. Cambridge University Press.
- CLIFT, R., GRACE, J. R. & WEBER, M. E. 1978 *Bubbles, Drops and Particles*, p. 154. Academic Press.
- EDWARDS, D. A., SHAPIRO, M., BAR-YOSEPH, P. & SHAPIRA, M. 1990 The influence of Reynolds number upon the apparent permeability of spatially periodic arrays of cylinders. *Phys. Fluids A* **2**, 45.
- ERGUN, S. 1952 Fluid flow through packed columns. *Chem. Engng Prog.* **48**, 93.
- FENG, J., HU, H. H. & JOSEPH, D. D. 1994 Direct simulation of initial value problems for the motion of solid bodies in a Newtonian fluid. Part 1. Sedimentation. *J. Fluid Mech.* **261**, 95.
- FISHER, T. S., TORRANCE, K. E. & SIKKA, K. K. 1997 Analysis and optimization of a natural draft heat sink system. *IEEE Trans. Components Packaging, Manufacturing Technol. A* **20**, 111.
- FRISCH, U., HASSLACHER, B. & POMEAU, Y. 1986 Lattice gas automata for the Navier–Stokes equation. *Phys. Rev. Lett.* **56**, 1505.
- GHADDAR, C. K. 1995 On the permeability of unidirectional fibrous media: A parallel computational approach. *Phys. Fluids* **7**, 2563.
- HASIMOTO, H. 1959 On the periodic fundamental solutions of the Stokes equations and their application to viscous flow past a cubic array of spheres. *J. Fluid Mech.* **5**, 317.
- HINCH, E. J. 1977 An averaged-equation approach to particle interactions in a fluid suspension. *J. Fluid Mech.* **83**, 695.
- HOWELLS, I. D. 1974 Drag due to the motion of a Newtonian fluid through a sparse array of small fixed objects. *J. Fluid Mech.* **64**, 449.

- KANEDA, Y. 1986 The drag on a sparse random array of fixed spheres in flow at small but finite Reynolds number. *J. Fluid Mech.* **167**, 455.
- LADD, A. J. C. 1994*a* Numerical simulations of particulate suspensions via a discretized Boltzmann equation. Part 1. Theoretical foundation. *J. Fluid Mech.* **271**, 285.
- LADD, A. J. C. 1994*b* Numerical simulations of particulate suspensions via discretized Boltzmann equation. Part 2. Numerical results. *J. Fluid Mech.* **271**, 311.
- LADD, A. J. C. & FRENKEL, D. 1990 Dissipative hydrodynamic interactions via lattice-gas cellular automata. *Phys. Fluids A* **2**, 1921.
- MEI, C. C. & AURIAULT, J.-L. 1991 The effect of weak inertia on flow through a porous medium. *J. Fluid Mech.* **222**, 647.
- NOBLE, D. R., GEORGIADES, J. G. & BUCKIUS, R. O. 1997 Interstitial hydrodynamics of steady inertial flows in large randomly packed beds. *J. Fluid Mech.* (submitted).
- SANGANI, A. S. & ACRIVOS, A. 1982 Slow flow past periodic arrays of cylinders with applications to heat transfer. *Intl J. Multiphase Flow* **8**, 193.
- SANGANI, A. S. & DIDWANIA, A. K. 1993 Dynamic simulations of flows of bubbly liquids at large Reynolds numbers. *J. Fluid mech.* **250**, 307.
- SANGANI, A. S. & MO, G. 1994 Inclusion of lubrication forces in dynamic simulations. *Phys. Fluids* **6**, 1653.
- SANGANI, A. S., MO, G., TSAO, H.-K. & KOCH, D. L. 1996 Simple shear flows of dense gas-solid suspensions at finite Stokes numbers. *J. Fluid Mech.* **313**, 309.
- SANGANI, A. S. & YAO, C. 1988 Transport processes in random arrays of cylinders. II. Viscous flow. *Phys. Fluids* **31**, 2435.
- SPIELMAN, L. & GOREN, S. L. 1968 Model for predicting pressure drop and filtration efficiency in fibrous media. *Environ. Sci. Tech.* **2**, 279.
- TAMADA, K. & FUJIKAWA, H. 1957 The steady two-dimensional flow of viscous fluid at low Reynolds numbers passing through an infinite row of equal parallel circular cylinders. *Q. J. Mech. Appl. Maths* **10**, 425.
- VERLET, L. & LEVESQUE, D. 1982 Integral equations for classical fluids. III. The hard disc system. *Mol. Phys.* **46**, 969.
- WILLIAMSON, C. H. K. 1996 Vortex dynamics in the cylinder wake. *Ann. Rev. Fluid Mech.* **28**, 477.
- YUSOF, J. F. 1996 Interaction of massive particles with turbulence. PhD thesis, Cornell University.